Unveiling the elusive roles of Cu species in determining the hydrocarbon trap performance during cold start in Cu-impregnated MFI type zeolites

Jinseong Kim [a,1], Jaehee Shim [a,1], Jin Chul Kim [b,1], Eunhee Jang [c], Jeong Hyeon Lee [b], Hionsuck Baik [d], Chun Yong Kang [c], Chang Hwan Kim [e], Kwan-Young Lee [a], Sang Kyu Kwak [a,*], Jungkyu Choi [a,*]

[a] Department of Chemical and Biological Engineering, Korea University, 145 Anam-ro, Seongbuk-gu, Seoul 02841, Republic of Korea
[b] School of Energy and Chemical Engineering, Ulsan National Institute of Science and Technology (UNIST), 50 UNIST-gil, Ulsan 44919, Republic of Korea
[c] Battery Performance Technology Development Team, Hyundai Motor Company, Hwaseong-si, Gyeonggi-do 18280, Republic of Korea
[d] Korea Basic Science Institute, Seoul Center, 145 Anam-ro, Seongbuk-gu, Seoul 02841, Republic of Korea
[e] Battery Development Center, Hyundai Motor Company, Hwaseong-si, Gyeonggi-do 18280, Republic of Korea

ARTICLE INFO

ABSTRACT

High-performance zeolite-based hydrocarbon (HC) traps were developed by impregnating MFI zeolites with Cu species. The corresponding cold-start test (CST) results revealed that the optimal Cu loading (ca. 5–7 wt%) led to high CST performance. To the best of our knowledge, our unprecedented complementary investigation based on both experimental and theoretical approaches revealed that Cu^+ ions rather than Cu^{2+} ions were key for securing high HC adsorption (especially propene) in the presence of copious amounts of water vapor. Moreover, tiny CuO nanoparticles (≤ 4 nm) on the exterior zeolite surface resulted in effective HC oxidation. This preferential HC adsorption and oxidation synergistically contributed to effective hydrocarbon trapping, making the Cu-impregnated MFI zeolites active HC traps. However, after hydrothermal treatment, a lower Cu content (3 wt% instead of 5–7 wt%) was rather desirable for preserving the marked CST performance, indicating that the original physicochemical properties were more damaged at higher Cu content.

1. Introduction

The content of the exhaust streams of internal combustion engine automobiles is strictly regulated. As a result, the development of highly efficient purification systems is urgently required. Currently, gasoline vehicles are equipped with a three-way catalyst (TWC) that can treat hydrocarbons, CO, and NO_x together at high temperatures (generally above ca. 300 °C) [1–8]. However, among the three main components of exhaust gas, unconverted hydrocarbons (HCs) are known to be released in significant quantities (up to ca. 80% of the total amount of HCs) before the TWC is thermally activated, that is, during the so-called cold-start period [4,9–11]. Thus, many studies investigating methods to eliminate HCs from the exhaust gas in the cold-start period are underway. To achieve this, a HC trap that adsorbs unconverted hydrocarbons at low temperatures and releases them at high temperatures has been proposed [9,12–18]. Although this concept is very simple, it is

quite challenging to achieve an HC trap having a high adsorption capacity, reasonable desorption temperature, and hydrothermal stability altogether for real uses [4,9,19]. Zeolites are considered good candidates for use as HC traps, especially because the structure of the zeolite can be selected according to the target adsorbate [4,9,10,13–16,20,21]. However, when using a zeolite alone, despite the large number of adsorption sites in the micropores, the target compounds (e.g., propene and toluene, which are representative HCs in the exit stream of the gasoline vehicles [13,22,23]) are easily desorbed from the adsorption sites before reaching high temperatures and can even slip out of the zeolite without being adsorbed [24,25].

To overcome these limitations, transition and precious metals have been loaded onto bare zeolites, resulting in effective HC trapping. In particular, Cu species loaded in zeolites in the form of cations were effective for adsorbing light hydrocarbons (e.g., propene) in the presence of water vapor in the feed [13,23–25]. Furthermore, the CuO

particles that are co-generated with the Cu cations facilitated oxidation at low temperatures [24–26]. In contrast to the clear roles of the CuO particles, the roles of the Cu cation species in HC adsorption remains unclear. Recent studies have suggested a plausible correlation between the amount of Cu cations and the cold-start test (CST) efficiency [24,25, 27]. Nevertheless, the exact roles of the Cu cations in HC adsorption (especially light hydrocarbon; propene) have not been determined, even though understanding their roles is critical for the design of robust, high-performance zeolite-based HC traps.

In this study, we clarified the elusive roles of the Cu species in Cu-impregnated zeolites in the HC-trap performance with respect to propene and toluene. In particular, we used an MFI type zeolite (or MFI zeolite) as the HC trap support because this serves as a good model for understanding the effect of porous supports [28–33]. Further, the Cu loading was systematically varied up to approximately 10 wt%. Subsequently, the morphological and structural properties of pristine MFI zeolite and its Cu-impregnated forms were investigated. In addition, we conducted CSTs under stoichiometric feed conditions ($\lambda = 1$) in the presence of a copious amount of water vapor (ca. 10 vol%) and the optimal Cu loading for high-performance HC removal was identified. In addition, the roles of the Cu cations (Cu^+ or Cu^{2+}) and CuO particles were investigated by decoupling the HC adsorption and oxidation abilities of the Cu-impregnated MFI zeolite. Moreover, Fourier transform infrared (FT-IR) spectroscopy with CO, NO, and pyridine probe molecules allowed for a quantitative comparison of Cu^+ and Cu^{2+} ions, as well as the acid sites, which are supposed to accommodate the Cu cations, before and after Cu impregnation. Based on these results, we were able to identify the relationship between Cu cations and amounts of adsorbed propene. The experimental investigation was complemented using density functional theory (DFT) calculations and grand canonical Monte Carlo (GCMC) simulations to elucidate the effect of cation types (especially, H^+, Cu^+, and Cu^{2+}) on the adsorption of propene and toluene in the absence and presence of water vapor. In addition, the oxidation ability of the Cu-impregnated zeolites, along with CuO particle-containing samples, was investigated to elucidate the role of CuO particles in HC oxidation. In particular, the HC trap samples that showed marked CST performance were used for rigorous understanding of their oxidation abilities by varying temperatures from 70° to 300°C. Furthermore, hydrothermal treatment (HT) under harsh conditions (air flow of 100 000 mL•g^{-1}•h^{-1} containing 10 vol% water vapor at 800 °C for 12 h) was performed on the Cu-impregnated MFI zeolites to investigate their hydrothermal stabilities. Finally, the relationship between the amount of adsorbed propene and the number of Cu^+ ions was confirmed for both fresh and hydrothermally treated Cu-impregnated MFI zeolites. To the best of our knowledge, we, for the first time, elucidated the elusive role of Cu cations on HC adsorption (in particular, propene) under the aforementioned stoichiometric feed conditions by interpreting the experimental and theoretical results in a complementary manner.

2. Experimental

Full characterization of the samples prepared in this study is provided in Subsection S1 of the Supporting Information.

2.1. Preparation of Cu-impregnated MFI zeolites as HC traps

H$^+$-MFI zeolites (SiAl = 11.5) were prepared by calcining commercial NH$_4^+$-MFI zeolite (SiO$_2$/Al$_2$O$_3$ = 23, Zeolyst International, CBV 2314) in a muffle furnace with 500 mL·min^{-1} air flow for 12 h. This allowed for the conversion of NH$_4^+$ ions to H$^+$ ions, creating acidic sites in the MFI zeolite structure. A wet impregnation method was then used to synthesize Cu-impregnated MFI zeolites. Details of the synthetic method can be found in the literature [24,25]. Various Cu-impregnated MFI zeolites were prepared by changing the amount of the copper precursor (copper nitrate trihydrate; Cu(NO$_3$)$_2$·3 H$_2$O, 98%, Sigma-Aldrich;

product number: 61197) to control the amount of loaded Cu in each sample. The resulting samples were labeled Cu(x) (x = 0, 1, 3, 5, 7, and 10), where x indicates the nominal weight percentage of Cu in the sample; in this case, Cu(0) represents the pristine H$^+$-MFI zeolite (i.e., no Cu impregnation).

2.2. Hydrothermal treatment (HT) on the HC trap

The prepared fresh samples (Cu-impregnated MFI zeolites; labeled Cu(x)) were hydrothermally treated to investigate their stability. For hydrothermal treatment (HT), the sample was placed inside a tubular reactor in a tubular furnace and treated at 800 °C with air flow containing 10 vol% water vapor for 12 h. The space velocity during HT was ca. 100 000 mL·g^{-1}·h^{-1} based on the sample weight. After completing HT, the resulting samples are denoted by Cu(x)_HT, where HT stands for the 12-h hydrothermal treatment applied to a fresh Cu(x) sample.

2.3. Preparation of CuO-containing samples

Commercial CuO particles (< 50 nm, Sigma-Aldrich; product number: 544868) were physically mixed with the lab-synthesized SiO$_2$ particles (approximately 100 nm). Lab-synthesized SiO$_2$ particles were prepared according to a previously reported method [34]. In this study, a mixture of CuO and SiO$_2$ is named CuO(x)/SiO$_2$, where x represents the Cu wt% in the mixture.

2.4. Simulated cold-start tests

The HC-trap performance of the samples prepared in this study was measured according to a previously reported method [25]. Specifically, pelletized Cu-impregnated MFI zeolite (ca. 0.06 g of 150–250-μm-sized particles) was placed on quartz wool in the middle of a quartz tube reactor (inner diameter of ca. 6.9 mm). As a reference, a CuO-containing sample (i.e., CuO(7)/SiO$_2$) was also used for CST to evaluate the CST performance under the same conditions. Before conducting the CSTs, the samples were heated from room temperature to 600 °C at a ramp rate of ca. 20 °C·min^{-1} in 50 mL·min^{-1} He flow and the temperature of 600 °C was maintained for 30 min; detailed discussion about the pretreatment condition is provided in Subsection S2.1. The reactor temperature and flow rate of the inlet gas were controlled using a temperature controller (UP35A, Yokogawa) and mass flow controller (MFC, High Tech, Bronkhorst), respectively. The reactor temperature during CST was monitored and recorded using a thermocouple located beneath the quartz wool. After completing the heat treatment process, approximately 100 mL·min^{-1} of simulated exhaust gas was fed to the reactor continuously (162 ppm propene, 162 ppm toluene, 0.6% O$_2$, 0.19% H$_2$, 13.36% CO$_2$, 0.58% CO, 10 vol% H$_2$O, 500 ppm Ar, and He balance; denoted by "CST feed" hereinafter; Table S1). The exclusion of NO, which is usually contained in the exhaust gas of gasoline-powered vehicles, from the CST feed in this study is explained in Subsection S2.2. The resulting space velocity (i.e., the ratio of the total feed flow rate to the pellet sample weight) was equal to 100 000 mL·g^{-1}·h^{-1} (to the best of our knowledge, we used the highest space velocity for HC trapping, as compared with those in previous reports; Table S2). To simulate cold-start conditions, the temperature was maintained at 70 °C for 5 min, heated to 600 °C at a ramp rate of 53 °C·min^{-1}, and maintained at 600 °C for 5 min. In particular, the simulated CST feed was designed to achieve a lambda value of 1, that is, stoichiometric condition. The concentrations of the outlet gas stream were analyzed using a mass spectrometer (MS, Lab Questor-RGA, Bongil) and gas chromatograph (GC) equipped with a flame ionization detector (YL6500, YL Instrument). The MS signals (m/z = 91 for toluene and 42 for propene) were monitored on line to track the concentrations of the outlet gases. For reliable measurements, Ar (500 ppm) was used as an internal standard. Along with MS, GC was used to monitor the concentration of total HCs in terms of the CH$_4$ reference. These two simultaneous measurements are

complementary and the MS- and GC-based measurements allowed for the chemical speciation of representative HCs (propene and toluene) and the total outlet HC amount, respectively. In fact, the GC-based measurement is desirable for reliable quantification of outlet HC amount regardless of the presence and absence of side products. To enable better comparison, we used the efficiency defined using Eq. (1), which represents the performance of the HC trap during CST measurements;

$$\text{Efficiency}\left(\%\right) = \left(1 - \frac{\int C_{\text{HC,outlet}}}{\int C_{\text{HC,inlet}}}\right) \times 100. \tag{1}$$

In short, the efficiency was calculated by subtracting the outlet concentrations of HCs (propene, toluene, and total HCs) in the exit stream ($C_{\text{HC,outlet}}$) from the corresponding inlet concentrations ($C_{\text{HC,inlet}}$) and integrating the differences up to 300 °C (temperature considered as an onset temperature of the TWC).

2.5. Breakthrough and oxidation tests

In addition to CSTs, breakthrough tests were conducted while maintaining the reactor temperature at 70 °C for 60 min under two different feed conditions. One was identical to the CST feed condition, whereas the other comprised HCs, Ar, water vapor, and He balance without O_2, CO_2, CO, and H_2; the latter is referred to as the HC feed and the detailed conditions are summarized in Table S1. These breakthrough tests were carried out to estimate the amount of adsorbed HCs (especially for the less adsorbed molecule, propene). The amount of adsorbed HCs was calculated until the outlet concentration of propene equaled the inlet concentration. Finally, to compare the oxidation ability of the Cu-impregnated MFI zeolites, oxidation tests under stoichiometric conditions (identical to those used for CST) were conducted at 300 °C (regarded as the onset temperature for activating TWCs) for 60 min. Furthermore, the Cu-impregnated zeolite samples (i.e., Cu(5) and Cu(7)) that showed the best CST performance in this study were used to investigate their oxidation abilities at lower temperatures (70, 110, 160, 210, 240, and 270 °C) for 60 min, while CuO(7)/SiO₂ was used as a reference sample. The conditions used for the CST, breakthrough test, and oxidation test are summarized in Table S3.

2.6. Preparation of water-saturated Cu-impregnated MFI zeolite

A pelletized Cu(5) sample (ca. 0.06 g of 150–250-μm-sized particles) was placed on quartz wool in the middle of a quartz tube reactor (inner diameter of ca. 6.9 mm). After it was pretreated as done for CST measurements, the temperature was set to 70 °C and the sample was exposed to 100 mL·min⁻¹ of a feed comprising 10 vol% of water vapor and balanced He for 30 min. This was attempted to saturate the sample with water to serve as a reference in evaluating the TGA results.

3. Computational modeling and details

Grand canonical Monte Carlo (GCMC) simulations were used to understand the adsorption of water vapor (ca. 10 kPa) during CST measurements. For this, eight Si atoms in the MFI zeolite framework were replaced by the same number of Al atoms and four Cu atoms were placed near the Al atoms. This replacement resulted in a Si/Al ratio of 11, which is comparable to the experimental Si/Al ratio of ca. 11.5. Subsequently, the unit cell model was extended to a $2 \times 2 \times 2$ supercell for the GCMC simulations. For the convenience, this is referred to as a Cu^{2+}-MFI crystal model. To identify the amount and location of water molecules adsorbed in the Cu^{2+}-MFI model at 70 °C and 10 kPa water vapor, GCMC simulations were conducted using a sorption program [35]. The potential energy parameters for all atoms were described by the COMPASS force field [36]. The GCMC simulations were performed with 1×10^6 equilibrium steps and subsequent same number of production steps.

In addition, density functional theory (DFT) calculations were conducted to comprehend the adsorption characteristics of water, propene, and toluene in the MFI zeolites under dry and wet conditions. To estimate the adsorption strengths of water, propene, and toluene molecules on the H^+, Cu^+, and Cu^{2+} ion-exchanged MFI zeolites, spin-polarized relativistic all-electron DFT calculations were carried out using the Dmol³ program [37,38]. For comparison, the adsorption energies of CO, which is contained with hydrocarbons in emissions from gasoline-powered vehicles, on the Cu^+ ions were also calculated under dry and wet conditions. The electron exchange-correlation energy was calculated using the generalized gradient approximation (GGA) and the Perdew-Burke-Ernzerhof (PBE) functional [39]. In addition, a double numerical plus polarization (DNP 4.4) basis set was chosen to describe the electronic wavefunction. To include dispersion effects corresponding to van der Waals interactions, the Tkatchenko-Scheffler scheme was used [40]. The convergence criteria for the energy, maximum force, and maximum displacement were set to 1.0×10^{-5} Ha, 0.002 Ha•Å⁻¹, and 0.005 Å, respectively. In addition, the Conductor-like Screening Model (COSMO) solvation method was adopted to describe the solvation environment under wet conditions; the dielectric constant of water (ε) used for these calculations was 78.54 [41].

In the DFT calculations, we employed a cluster model of the MFI zeolite (i.e., MFI 46 T cluster model) that included the intersection of two channels in the MFI crystal. A model similar to this cluster model was reported in a previous study [42]. The H^+-MFI 46 T cluster model was prepared by replacing two Si atoms with the same number of Al atoms to ensure the most stable Al position, followed by the addition of protons to neutralize the framework. Based on this H^+-MFI 46 T cluster model, Cu^+- and Cu^{2+}-MFI 46 T cluster models were prepared by exchanging one proton for one Cu^+ ion and two protons for one Cu^{2+} ion, respectively. A partial optimization procedure was employed for all H^+-, Cu^+-, and Cu^{2+}-MFI 46 T cluster models [43,44].

4. Results and discussion

4.1. Morphological and structural properties of Cu-impregnated MFI zeolites

The Cu/Al ratios and Cu wt% estimated from scanning electron microscopy (SEM)/energy dispersive X-ray spectroscopy (EDX) mapping of the Cu-impregnated MFI zeolites (Figs. S1-S3) are summarized in Tables S4-S5. Considering that the EDX could have a possible limit regarding the bulk composition, we attempted to cover particles as many as possible at low magnification SEM images shown in Figs. S2-S3 for acquiring the representative composition. The results indicate that the amount of Cu in the HC trap increased with increase in the amount of loaded Cu. Fig. 1a1-a3 shows that Cu was uniformly distributed in the MFI zeolite support and large Cu species (seemingly CuO particles, indicated by the red-dashed ellipses in Fig. 1a2-a3) were observed. Further, the size of the particles on the outer surface increased with increase in Cu loading. In addition, the transmission electron microscopy (TEM) images in Fig. 1b1-b3 revealed the presence of tiny CuO particles (indicated by red arrows in Fig. 1b1-b3); the full TEM images are shown in Fig. S4. However, when the Cu loading amount was very low (1 wt%), these tiny CuO particles were not formed (Fig. S4b2), suggesting that a threshold amount was required to generate additional CuO particles on the outer surface because the majority of the Cu precursor penetrated the zeolite pores and was transformed into Cu cations.

In Fig. 1c1-c2, the XRD patterns of Cu(x) (x = 0, 1, 3, 5, 7, and 10) in the range of 5° − 40° are displayed along with the simulated XRD pattern of CuO (represented by ▼) on top. The XRD analysis indicated that the original zeolite structure was not affected by Cu impregnation. In addition to the zeolite structure, the XRD patterns of the high-Cu-loading samples (i.e., Cu(5), Cu(7), and Cu(10)) contained reflections consistent with the (002)/(11$\bar{1}$) planes of CuO particles (larger than
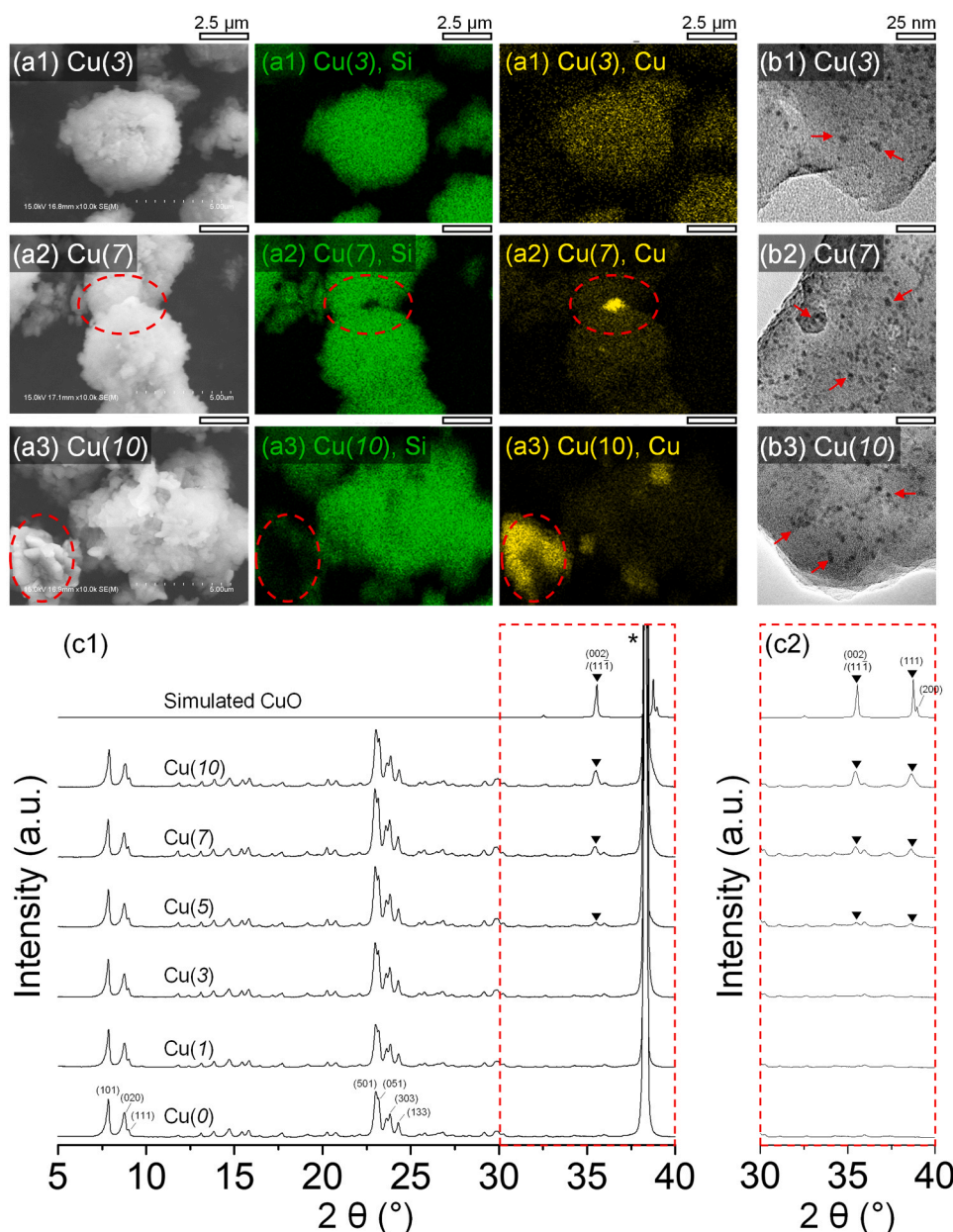
Fig. 1. (a1)-(a3) SEM (1st column) and SEM/EDX mapping (2nd and 3rd columns) images of Cu(x) (x = 3, 5, and 7) along with (b1)-(b3) TEM images (4th column). The results for other Cu(x) (x = 0, 1, and 10) samples are shown in Figs. S1 and S4 along with those shown in (a1)-(a3) and (b1)-(b3). Red-dashed ellipses and red arrows indicate CuO particles in (a2)-(a3) and (b1)-(b3), respectively. The scale bars in (a1)-(a3) and (b1)-(b3) indicate 2.5 μm and 25 nm, respectively. (c1) XRD patterns of Cu(x) (x = 0, 1, 3, 5, 7, and 10) measured by using (c1) an aluminum holder. The 2θ range marked by the red-dashed rectangles in (c1) was measured again by using a quartz holder and the corresponding XRD patterns are shown in (c2). In (c1)-(c2), for comparison, the simulated XRD pattern of CuO phases is added on top and the black reverse triangles (▼) are added to indicate the XRD peaks owing to the CuO phases. In (c1), an asterisk (*) indicates a XRD peak arising from the aluminum holder.

4 nm, as reported in the literature [22,31]) at ca. 35.5°. For the three samples, the degree of CuO phase formation monotonically increased with increase in Cu content. Considering that an additional peak corresponding to the (111) plane of the CuO phase at ca. 39° overlapped with the XRD peak of the Al holder (denoted by an asterisk), XRD patterns from 30° to 40° were obtained in a quartz holder to understand the CuO phases better. Fig. 1c2 clearly revealed that above a certain Cu loading (i.e., 5 wt%), CuO particles were formed and their proportions increased with increase in Cu loading.

Combining the results obtained from the SEM images, SEM/EDX maps, TEM images, and XRD patterns, we concluded that agglomerated, large CuO particles were formed in the samples having high Cu loadings (i.e., Cu(x); x = 5, 7, and 10) and their size monotonically increased with increase in Cu loading. Although bulk phase XRD analysis could not detect the presence of small CuO particles (≤ 4 nm) [22,31], tiny CuO particles were observed on the outer surface of Cu(3). This indicates that above some critical Cu loading (here, 3 wt%), tiny CuO particles could be formed on the outer surface and, in the case of excessive Cu loading, the agglomeration was pronounced, leading to the formation of large

CuO particles. In addition, the structural properties of fresh HC traps were investigated via Ar physisorption (more information is provided in Subsection S2.3; please refer to Table S4 and Figs. S5-S7 for details). The Ar physisorption measurements showed that Cu impregnation of the MFI zeolite reduced the surface area and pore volume, and the difference before and after Cu impregnation increased with increase in Cu loading.

4.2. CST performance of the Cu-impregnated MFI zeolites

Based on the morphological and structural properties of the Cu-impregnated MFI zeolites, their CST performances were investigated (Fig. 2 and S8). For conciseness, the results for the bare MFI zeolite (i.e., Cu(0)) and Cu-impregnated MFI zeolites at different nominal Cu loadings of 3, 7, and 10 wt% are shown in Fig. 2a, c, and e; all the results are displayed in Fig. S8. As reported previously [24], the bare MFI zeolite (Cu(0)) did not have the ability to adsorb propene in the presence of water vapor, but Cu impregnation resolved this issue. In contrast, all samples (even the bare MFI zeolite) showed good toluene adsorption, suggesting that toluene adsorption on the MFI zeolite was insensitive to
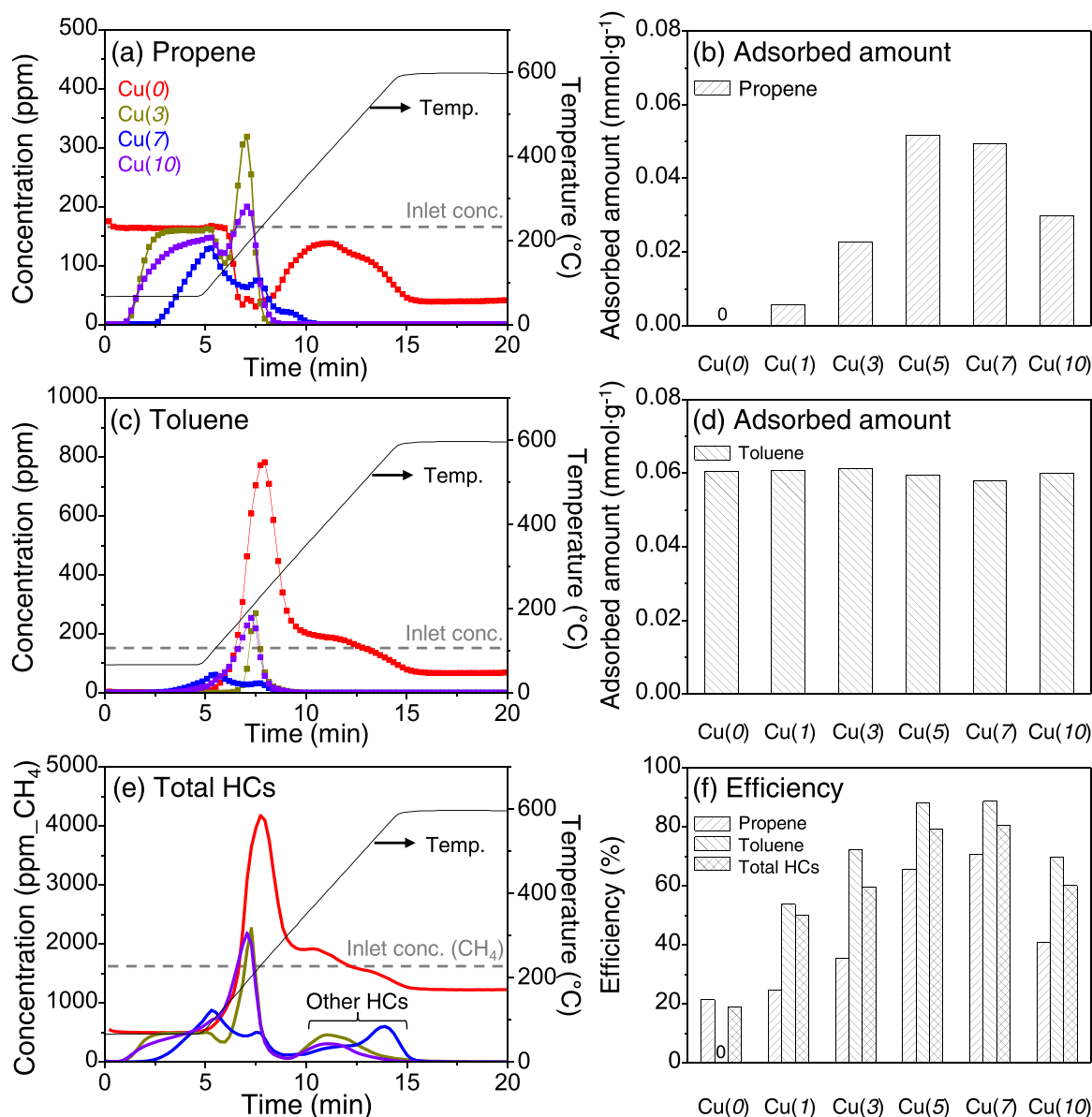
Fig. 2. CST results of Cu(x) (x = 0, 3, 7, and 10) with respect to (a) propene, (c) toluene, and (e) total HCs in terms of CH₄. The additional results of other Cu(x) (x = 1 and 5) are shown in Fig. S8 along with those shown in (a), (c), and (e). In (a), (c), and (e), the gray-dashed lines indicate the inlet concentrations of (a) propene, (c) toluene, and (e) total HCs in terms of CH₄. In (b) and (d), the amounts of adsorbed propene and toluene were calculated from the exit concentration profiles in (a) and (c), respectively, up to 5 min. For convenience, in (e), some other HCs produced during CST are indicated by a brace. In addition, the CST efficiencies of Cu(x) (x = 0, 1, 3, 5, 7, and 10) are shown in (f). In (b) and (f), "0" for Cu(0) indicates that adsorbed amount and efficiency are zero. All the original CST results of Cu(x) (x = 0, 1, 3, 5, 7, and 10) are displayed in Fig. S8.

the cation type in the zeolite structure (additional information regarding the desorption temperature of HCs is given in Subsection S2.4). Nevertheless, the Cu(0) sample desorbed the already adsorbed toluene to a large extent compared to Cu-impregnated MFI zeolites (Fig. 2c). Furthermore, Cu(0) could not remove toluene at high temperatures, unlike the Cu-impregnated MFI zeolites, which could oxidize toluene (Fig. 2c). Thus, these results underline the desirable effect of Cu impregnation on active HC trapping. Intriguingly, as shown in Fig. 2e, an additional desorption peak (indicated by a brace) appeared between ca. 10–15 min, though propene and toluene were not detected (Fig. 2a and c). This peak was ascribed to side products (e.g., methane and benzene) from propene and toluene at high temperatures (ca. 300–350 °C); detailed information is provided in Subsection S2.5 (please refer to Fig. S9). Furthermore, to verify the regenerative ability of Cu-impregnated MFI zeolites, three consecutive CST measurements of Cu(5) as well as Cu(0) were conducted (refer to Fig. S10) and the

corresponding information is provided in Subsection S2.6. In addition, the thermogravimetric analysis results of the samples recovered from the CST measurements indicated the oxidative properties of the Cu-impregnated MFI zeolites, as reflected by the plateau region at temperatures higher than 300 °C (refer to Subsection S2.7 and Fig. S11).

For comparison, the amounts of adsorbed propene and toluene are shown in Fig. 2b and d, respectively, and the CST efficiencies with respect to propene, toluene, and total HCs (in terms of CH₄) are shown in Fig. 2 f. In particular, among the prepared samples, Cu(5) showed the maximum propene adsorption ability when the first 5 min of CST was used to estimate the propene adsorption (Fig. 2b). As the Cu loading increased, the corresponding propene adsorption ability increased, reaching a maximum for Cu(5), and then decreased again. This result reveals that at higher than 5 wt% Cu loading, other Cu species that were not responsible for propene adsorption were formed. At this moment, we would like to mention that despite the high CO concentration (0.58% vs.

162 ppm propene) in the CST feed, the effective adsorption of propene was feasible, indicating a superior feature of Cu-impregnated MFI zeolites. As expected from the CST performance, the amounts of toluene adsorbed by the prepared samples were comparable (Fig. 2d). However, considering that HC traps should desorb the already adsorbed HCs at the high temperatures at which the TWC is activated [1–7], the bare MFI zeolite was not appropriate for HC trapping. The net ability to eliminate HCs up to 300 °C is defined by the CST efficiency (see Eq. (1)) and as shown in Fig. 2 f, the optimal Cu loading (in this study, 5–7 wt%) was required to achieve the maximum performance. The CST performance shown in Fig. 2 clearly shows the importance of an appropriate Cu loading for producing Cu species that are active for HC adsorption and oxidation.

4.3. Cu oxidation state and quantification for the Cu-impregnated MFI zeolites

Having determined the CST performance of the Cu-impregnated MFI zeolites, we attempted to correlate this with the corresponding chemical properties to enable the design of HC traps. To elucidate the chemical properties, we used FT-IR-based Cu speciation using NO and CO as the probe molecules. To ensure a fair comparison, all FT-IR spectra were normalized by the pellet weight ($w_{pellet} \approx 0.01$ g), thus yielding a specific absorbance (denoted by $A(\nu)/w_{pellet}$). Furthermore, the specific absorbance area (denoted by $\int A(\nu)d\nu/w_{pellet}$) was calculated by integrating the specific absorbance peak [45]. The thermal activation of Cu-impregnated MFI zeolites in He flow leads to the formation of three main Cu species (Cu^+ and Cu^{2+} ions and CuO particles) because the other plausible Cu species ($[Cu-OH]^+$ and $[Cu-O-Cu]^{2+}$ ions) are reduced to Cu^+ ions after activation in He flow or a vacuum [33,46,47].

For Cu speciation, NO-adsorption FT-IR analysis was conducted. NO molecules can be attached to Cu^+, Cu^{2+}, and CuO in Cu-loaded zeolites and, thus, the corresponding FT-IR spectra can be used to distinguish them [28,48]. Unfortunately, NO molecules can also react with Cu cations and turn into other molecules while changing the Cu states; thus, it is quite challenging to measure the amount of saturated NO molecules [28,49]. Therefore, to minimize unwanted reactions and trace changes with measurement time, a small amount of NO (5 mL·min^{-1} of 500 ppm of NO with He balance) was fed into the FT-IR cell, the cell temperature was maintained at 0 °C using a circulator, and NO-adsorption FT-IR spectra were recorded every 15 s. The subsequent decoupling of the resulting spectra based on the IR peaks around $\nu_{max} = 1910$, 1895, and 1810 cm^{-1}, which correspond to Cu^{2+}-NO, CuO-NO, and Cu^+-NO, respectively, allowed the identification of the Cu species with time and a fair comparison of their transient quantities. The spectra recorded for Cu (x) ($x = 1, 3, 5, 7,$ and 10) at 1-min intervals from 0 to 30 min are shown in Fig. S12a1-e1. To ensure fair comparison, the FT-IR spectra of the Cu (x) ($x = 1, 3, 5, 7,$ and 10) samples displayed in Figs. 3a1 and S12a2-e2 correspond to those when the peak intensity at 1810 cm^{-1} owing to Cu^+-NO was maximized. The corresponding specific absorbance areas are displayed in Fig. 3a2 and the specific absorbance areas estimated up to 15 min are shown in Fig. S12a3-e3. Notably, the amounts of all three Cu species (Cu^+ and Cu^{2+} ions and CuO particles) monotonically increased with increase in Cu content from 1 to 3–5 wt% (Fig. 3a2).
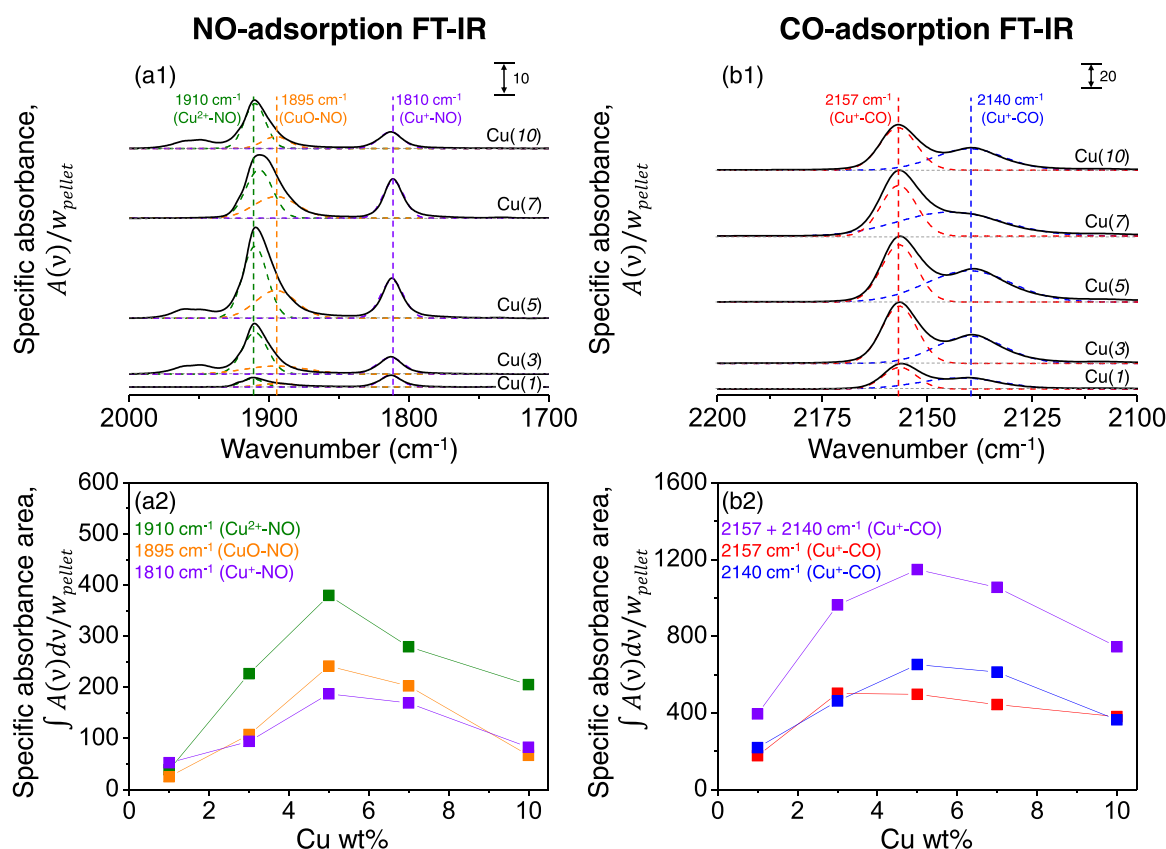
Fig. 3. (a1)-(b1) FT-IR spectra (top) and (a2)-(b2) the corresponding absorbance areas (bottom) of Cu(x) ($x = 1, 3, 5, 7,$ and 10) based on (a1)-(a2) NO and (b1)-(b2) CO molecules. In (a1), the spectra between 1860 and 1930 cm^{-1} were deconvoluted using the peaks around $\nu_{max} = 1910$ cm^{-1} (Cu^{2+}-NO; indicated by the green-dashed line) and $\nu_{max} = 1895$ cm^{-1} (CuO-NO; indicated by the orange-dashed line). In addition, in (a1), the peak around $\nu_{max} = 1810$ cm^{-1} that represents Cu^+-NO is indicated by the violet-dashed line. In (b1), all spectra in the range of ca. 2120–2165 cm^{-1} were deconvoluted using the peaks around $\nu_{max} = 2157$ cm^{-1} (Cu^+-CO; indicated by the red-dashed line) and $\nu_{max} = 2140$ cm^{-1} (other Cu^+-CO; indicated by the blue-dashed line). All deconvoluted peaks were fitted with Gaussian distribution curves and the deconvoluted peaks that account for the species described in (a1)-(b1) were further used to estimate the specific absorbance areas and the results are shown in (a2)-(b2). In (b2), the summation of two specific absorbance areas owing to Cu^+-CO is marked in violet.

Although the amount of CuO particles was maximized in Cu(*10*), which had the highest Cu content in this study (Figs. S1-S4), the amount of CuO particles detected was smaller (Fig. 3a2). Because NO molecules can interact with CuO particles on the outer surface, Cu(*10*), which apparently contained agglomerated CuO particles (Figs. 1a3, S1f, S2f, and S3f), yielded a smaller specific absorbance area than Cu(*5*) and Cu(*7*). This suggested that the CuO particles were smaller and better dispersed in Cu(*5*) and Cu(*7*). Finally, despite the similar transient trends for all three Cu species (Cu^+ and Cu^{2+} ions and CuO particles) (Fig. S12c3-d3), their amounts in Cu(*5*) were higher than those in Cu(*7*) (Fig. 3a2).

Because Cu^+ ions can react with NO molecules, even at 0 °C, and be converted into other Cu species, the FT-IR peak area arising from Cu^+-NO was not saturated, preventing the evaluation and comparison of the amounts of Cu species. In contrast, CO molecules are reliable probe molecules because they are adsorbed on Cu^+ ions only and, thus, can be used to compare the relative quantity of Cu^+ ions. Because Cu^+-$(CO)_x$ (x = 1, 2, and 3) can be formed at high CO concentrations, we focused on acquiring the CO-adsorption FT-IR spectra from only chemically attached Cu^+-CO, which were present after exposure to the CO-containing feed and subsequent 2-h evacuation [31,50–52]. The CO-adsorption FT-IR spectra are shown in Fig. 3b1. Similar to the NO-adsorption FT-IR analyses in Fig. 3a2, the specific absorbance areas were obtained from the CO-adsorption FT-IR spectra by deconvoluting the peaks around ν_{max} = 2157 and 2140 cm^{-1} (Fig. 3b2). Of the two peaks of Cu^+-CO, the peak at ν_{max} = 2157 cm^{-1} corresponds to the combined results of a blue shift due to a σ-donation from CO to Cu^+ ions and a red shift caused by a π-back donation from the D-orbitals of the Cu^+ ions to the π * anti-bonding orbitals of the CO. The other peak observed at ν_{max} = 2140 cm^{-1} corresponds to the further red-shifted peak from the peak at ν_{max} = 2157 cm^{-1} owing to the neutralization of Cu^+ ions by the framework oxygen in zeolites [53]. The summation results are also presented in Fig. 3b2. We noticed that the trend in the specific absorbance peak areas of the CO-adsorption FT-IR spectra (corresponding to Cu^+-CO) was comparable to that of the NO-adsorption FT-IR spectra (corresponding to Cu^+-NO) (Fig. 3a2). In summary, the amount of Cu^+ ions monotonically increased with increase in Cu content and the maximum value was observed for the sample containing 5 wt% Cu, after which the amount of Cu^+ ions decreased.

In particular, pyridine (Py)-based FT-IR analyses (Fig. S13), which can provide information regarding cation species indirectly [24,25,54], were not reliable for proper evaluation of Cu cations; detailed results and discussion about the Py-adsorption FT-IR analyses are provided in Subsection S2.8. Notably, the use of excess Cu in the zeolites inevitably resulted in the formation of CuO particles on the outer surface, in addition to ion-exchanged Cu cations (Fig. 1b and S4). However, CuO particles activated in a vacuum at high temperatures (e.g., higher than 500 °C) could contribute to the Py-adsorption IR peaks [55]. Consequently, both Cu cations and CuO particles yielded Py-adsorption FT-IR peaks. Furthermore, ion-exchanged cations can constrict the MFI channels (ca. 5.5 Å) and, thus, reduce the accessibility of pyridine (ca. 5.9 Å [56]) to the acid sites [57]. Therefore, the Py-based estimation of the numbers of B and L sites in pores of the MFI type zeolite having excessive Cu cations (here, Cu^+ or Cu^{2+} ions) would not be reliable. As a result, the direct interpretation of the B and L sites from the data in Fig. S13b cannot be used to provide quantitative information regarding Cu cations [58,59]. Nevertheless, the amount of L sites followed the trend observed in other characterizations (NO- and CO-adsorption FT-IR above) when Cu loading was low (i.e., Cu(*x*); x = 1, 3, and 5). Although the difference of Brønsted acid sites before and after Cu impregnation can be attempted to describe the adsorption property, the conventional Py-adsorption FT-IR analyses would not provide proper information regarding the Cu cations as mentioned above [24,25,54,55,57–59]. This will apply to Lewis acid sites as well. Furthermore, considering the inconsistent reports that pyridine can interact with Cu^+ or Cu^{2+} ions [58,59], the corresponding Lewis acid site-based correlation with CST performance needs elaborate analysis. In addition, propene, which was

used as one of the representative hydrocarbons during the CST, was used as another probe molecule for FT-IR-based Cu-speciation. In the propene-adsorption FT-IR spectra of Cu(*5*), the fact that propene can be adsorbed to the Cu^+ ions in the Cu-impregnated MFI zeolite even in the presence of water vapor was evidenced by the peak at 1543 cm^{-1} corresponding to Cu^+-propene [60] (please refer to Fig. S14).

In addition to the FT-IR analyses with multiple probe molecules, we conducted ultraviolet visible near-infrared (UV-Vis-NIR) analyses on the Cu-impregnated MFI zeolite after He activation. Although UV-Vis-NIR analyses can identify Cu^{2+} ions, the peak arising from Cu^{2+} ions (ν_{max} = 12,500 cm^{-1}) was highly overlapped with a broad peak arising from CuO particles (Fig. S15a-b) [61]. Therefore, we could not distinguish them properly when a high amount of CuO particles was present in the Cu-impregnated MFI zeolite sample (i.e., Cu(*7*) and Cu(*10*) in this study). Because of this overlap, we focused on investigating Cu-impregnated MFI zeolites with low Cu contents (i.e., Cu(*x*); x = 1, 3, and 5) that did not contain a considerable amount of CuO particles. It has been reported that the amount of Cu^{2+} ions linearly correlates with the peak area of each d-d transition peak after dehydration [62]. Indeed, the peak area around ν_{max} = 12,500 cm^{-1}, which corresponds to the d-d transition of Cu^{2+} ions in the dehydrated form of Cu-MFI zeolite, monotonically increased with increase in Cu content (Fig. S15c) [61]. Consistent with the NO-adsorption FT-IR results shown in Fig. 3a1-a2, UV-Vis-NIR analyses also indicated that the amount of Cu^{2+} ions increased with increase in Cu content up to 5 wt%. However, XPS analysis (Fig. S16) was not appropriate for the identification and quantification of Cu species in the Cu-impregnated MFI zeolites, apparently because it is an *ex-situ* method unlike FT-IR (Fig. 3 and S12-S14) and UV-Vis-NIR (Fig. S15) analyses and/or limited to characterize the element state on the outer surface [63–65].

4.4. Relationship between the Cu cations and propene adsorption for the Cu-impregnated MFI zeolites

In previous studies [24,25], we proposed that the amount of Cu^+ ions inside the zeolite was related to the propene adsorption capacity or CST efficiency. Because the CST performance is a coupled function of adsorption/desorption and oxidation, we attempted to deconvolute the respective performance and, thus, elucidate the roles of the Cu cations in HC adsorption and CuO particles in HC oxidation. For HC adsorption, especially for propene, the amount of adsorbed propene was almost linearly proportional to the amounts of both Cu^+ and Cu^{2+} ions (Fig. 2a-b, 3a2-b2, and S8). However, the desorbed propene concentration did not reach the inlet concentration in the initial 5 min at 70 °C during CST for some of the Cu-impregnated MFI zeolites (i.e., Cu(*5*), Cu(*7*), and Cu(*10*); Fig. 2a and S8). In other words, it was impossible to determine the saturated amount of propene from the CST results. Therefore, we extended the experimental duration to 60 min at 70 °C under CST feed conditions (Figs. 4a1 and S17); that is, we carried out breakthrough experiments. The breakthrough result in Fig. 4a1 clearly demonstrated the inability of Cu(*0*) to adsorb propene. As the Cu content increased, the corresponding propene adsorption increased for Cu(*1*) and Cu(*3*). However, Cu(*5*) and Cu(*7*) exhibited similar adsorption capacities, though the slope of the breakthrough curve was steeper for Cu(*5*). This implied that there was a difference in the adsorption strength. However, increasing the Cu content to 10 wt% (i.e., Cu(*10*)) resulted in a decrease in the amount of adsorbed propene. Furthermore, different breakthrough curve behavior was observed for Cu(*10*). However, considering that the presence of large amounts of other gases (e.g., CO adsorption onto Cu^+ ions) in the CST feed can considerably inhibit the adsorption of propene, the corresponding breakthrough measurement will be inaccurate. To overcome this limitation, the HC feed condition, where the permanent gas molecules of CO, CO_2, O_2, and H_2 were excluded from the CST feed, was used for breakthrough measurements. The corresponding results are shown in Figs. 4a2 and S18. The direct comparison of the breakthrough curve results shown in Fig. 4a1-a2
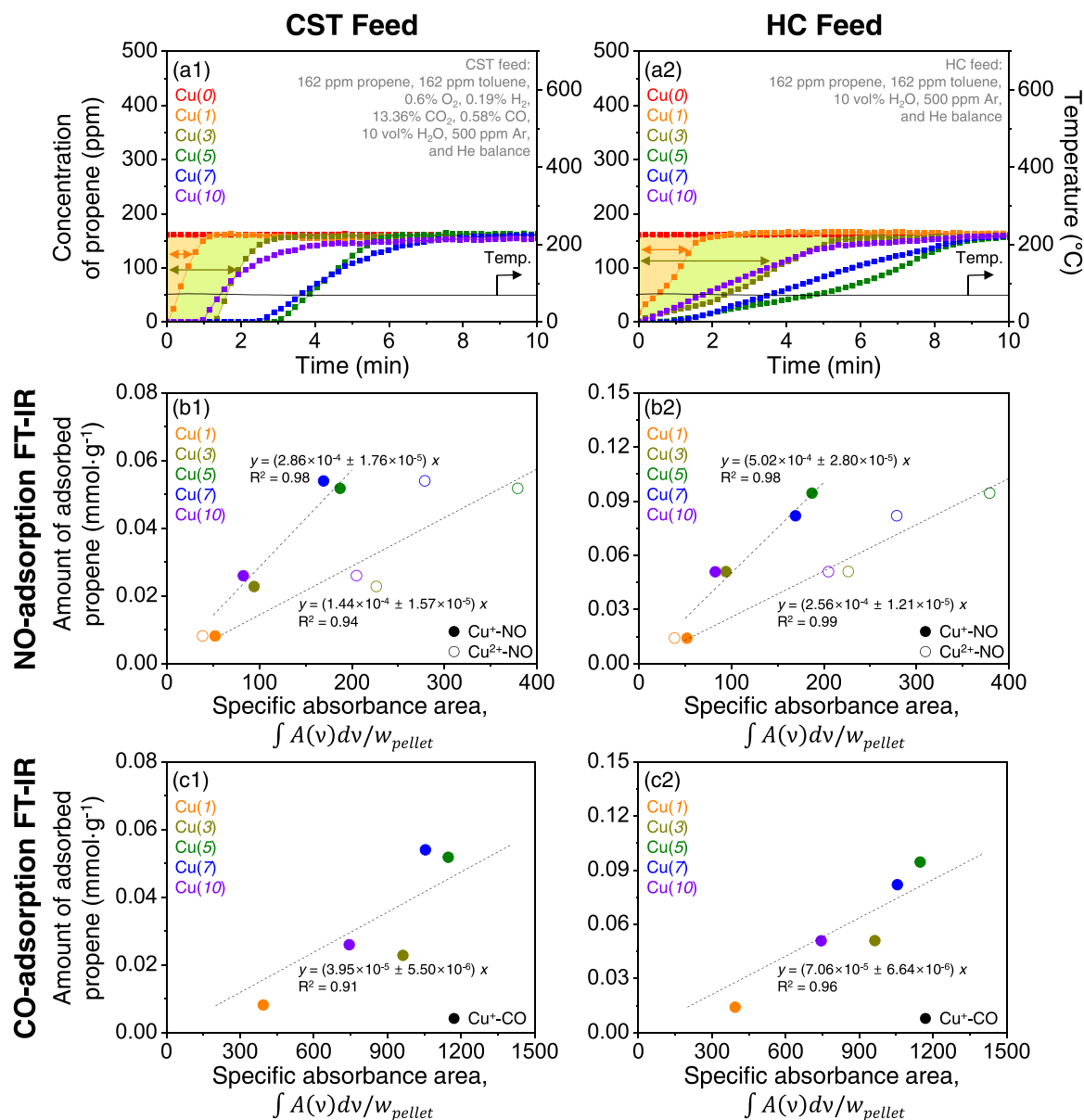
Fig. 4. (a1)-(a2) Breakthrough test results of Cu(x) (x = 0, 1, 3, 5, 7, and 10) at 70 °C using two different feeds: (a1) CST and (a2) HC feeds. In (a1)-(a2), the regions that were integrated to calculate the amounts of adsorbed propene in Cu(*1*) and Cu(*3*) are marked in orange and yellow green, respectively. The amount of adsorbed propene as a function of the specific absorbance area, along with the linear regression plots, are shown in (b1)-(c1) for the CST feed and in (b2)-(c2) for the HC feed. In (b1)-(b2), the specific absorbance areas corresponding to Cu^+-NO and Cu^{2+}-NO were obtained from Fig. 3a2, whereas in (c1)-(c2), those corresponding to Cu^+-CO were obtained from the summation of the two specific absorbance areas of Cu^+-CO in Fig. 3b2.

revealed that the exclusion of the aforementioned gas molecules from the feed was desirable for estimating the amount of adsorbed propene. Notably, the trends in the breakthrough curves were comparable for the Cu-impregnated MFI zeolites. In addition, the breakthrough tests under dry CST feed and dry HC feed conditions (shown in Figs. S19 and S20, respectively, and the detailed conditions are summarized in Table S1) were conducted for elaborate analyses of the adsorption rate and amount of propene. Despite the complicate gas composition (i.e., 0.6% O_2, 0.19% H_2, 13.36% CO_2, and 0.58% CO gases) in the CST feed, the adsorption rate of propene under CST feed conditions was slightly higher than that under HC feed conditions (Figs. 4a1-a2 and S21a1-b1). However, this trend was opposite to those measured under dry CST and HC feed conditions (Fig. S21a2-b2), as expected from possible inhibition of propene adsorption by other gases (mainly CO). Nevertheless, the amounts of adsorbed propene were smaller in all HC traps under CST feed compared to HC feed under both dry and wet conditions

(Fig. S21c1-c2). This clearly indicates that water vapor under HC feed conditions had a greater effect on decreasing the adsorption rate of propene, though additional decoupling of the effects of other gas components should be done for better understanding.

Furthermore, we conducted Cu speciation and quantification based on probe-molecule-adsorption FT-IR analyses to correlate the corresponding quantitative information with the amounts of adsorbed propene under CST and HC feed conditions. In particular, it appears that the amounts of adsorbed propene under both feed conditions were linearly proportional to those of Cu^+ and Cu^{2+} ions (estimated from the NO-adsorption FT-IR analyses; Fig. 4b1-b2) and Cu^+ ions (estimated from the CO-adsorption FT-IR analyses; Fig. 4c1-c2). Clearly, the statistical analyses, as reflected by the relatively smaller confidence interval values next to the estimated slopes in Fig. 4b1-b2 and c1-c2, indicated that the use of HC feed conditions enabled the reliable measurement of the amount of adsorbed propene. Nevertheless, it was challenging to

determine which Cu species (Cu$^+$ or Cu^{2+}) were responsible for propene adsorption in the presence of 10 vol% water vapor. Because the propene adsorption capacity of Cu(0) was technically nil (Fig. 2a and 4a1), it is reasonable to disregard the Brønsted acid sites as playing any role in HC trapping.

Rigorous characterization of the chemical properties (especially based on the Cu cation speciation/quantification) (Fig. 3a2-b2) and their correlation with the propene adsorption capacity under HC feed conditions in the breakthrough tests (Fig. 4a2) revealed that both Cu$^+$ and Cu^{2+} ions were important for the propene adsorption of the Cu-impregnated MFI zeolites (Fig. 4b2-c2). In fact, Cu(5), which had the highest concentrations of both Cu$^+$ and Cu^{2+} ions, showed the maximum propene adsorption capacity, whereas higher Cu loading led to lower formation of Cu cations (Fig. 3a2-b2). This could be attributed to the pronounced degree of formation of CuO particles on the outer surface; indeed, the adsorption capacity decreased for Cu(7) and Cu(10) (Fig. 4a2).

4.5. DFT calculations of the binding energies of water, propene, and toluene on different cations in MFI zeolites

Linear regression based on the NO-adsorption FT-IR analyses (Fig. 4b2) suggested that both Cu$^+$ and Cu^{2+} ions in the Cu-impregnated MFI zeolites could account for propene adsorption. It is known that propene adsorption onto Cu$^+$ and Cu^{2+} ions is due to π-back donation [58,66] and σ-donation [67,68], respectively. However, despite

substantial experimental efforts to clarify the roles of Cu cations inside zeolites in light hydrocarbon (e.g., propene) adsorption [12,23–25,27, 69], detailed elucidation to determine which Cu cations (Cu$^+$ or Cu^{2+} ions) were responsible for propene adsorption has not yet been conducted. Therefore, in this study, we further used DFT calculations for clarity.

Because the CSTs were carried out under wet conditions (about 10 vol% water vapor), the water adsorption behavior in Cu-impregnated MFI zeolites should be determined to understand their CST efficiency. For this, the water adsorption isotherms at 70 °C and up to 10 kPa (the same as the initial temperature for CST measurements) were obtained to estimate the amount of water in the zeolite pores. Fig. 5a shows that approximately 33 water molecules were adsorbed per MFI unit cell in Cu (0) at 70 °C and 10 kPa. However, the number of adsorbed water per MFI unit cell could not be calculated accurately for the Cu-impregnated MFI zeolites because it is difficult to determine the density of Cu-impregnated MFI zeolites after Cu impregnation. Nevertheless, the amounts of adsorbed water in mmol·g^{-1} were pronounced for all Cu-impregnated MFI zeolites. In parallel, GCMC simulations were conducted to predict the water adsorption amount. The GCMC simulation results shown in Fig. 5b and S22-S23 reveal that approximately 30 water molecules on average were adsorbed per unit cell of Cu-MFI zeolite at the same temperature (70 °C), which agrees well with the experimental results shown in Fig. 5a. Therefore, it was reasonable to assume that when the CST feed containing 10 vol% water vapor passed through the Cu-impregnated MFI zeolite, a copious amount of water was adsorbed
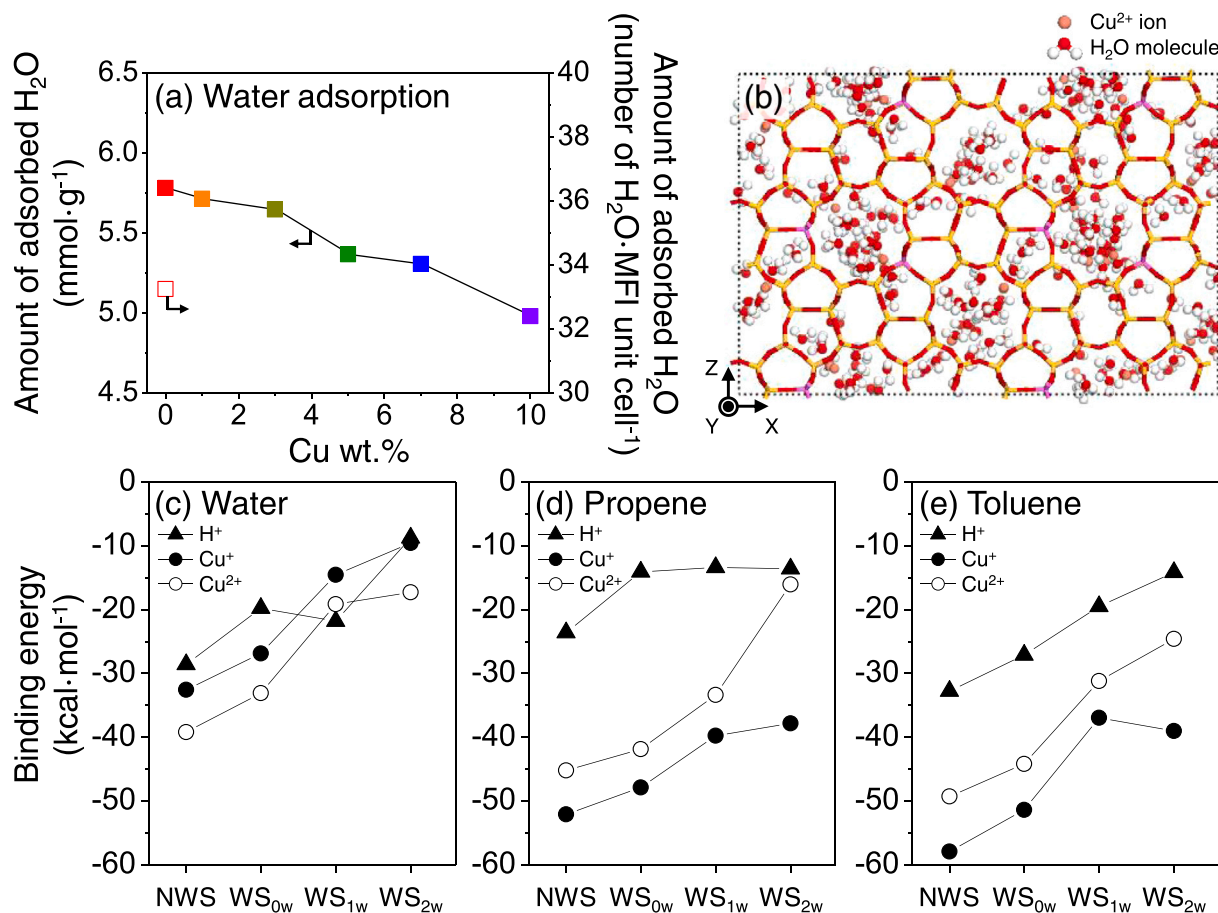
Fig. 5. Amounts of adsorbed water molecules in (a) Cu(x) (x = 0, 1, 3, 5, and 10) at 70 °C and 10 kPa water vapor. (b) Projection (along the y-axis) of the most stable water adsorption configuration in the Cu^{2+}-MFI crystal model obtained by GCMC simulations. Another projection result is shown in Fig. S23. (c)-(e) Binding energies of (c) water, (d) propene, and (e) toluene under dry and wet conditions (NWS; no water solvation, WS$_{0w}$; water solvation only, WS$_{1w}$; water solvation with one explicit water molecule, and WS$_{2w}$; water solvation with two explicit water molecules) on H$^+$, Cu$^+$, and Cu^{2+} ions. In (b), for clarity, the zeolite framework except cations is displayed in a stick model, and cations and water molecules are presented by a ball-and-stick model. In addition, Al, Si, O, and H atoms are colored in pink, yellow, red, white, and orange, respectively. In particular, Cu^{2+} ions are represented by orange spheres.

on the zeolite support and this is, thus, likely to have a significant effect on the adsorption behavior of HC molecules.

In this study, the binding energies between the cations (i.e., H^+, Cu^+, and Cu^{2+}) and adsorbed molecules (i.e., water, propene, and toluene) relevant to HC trapping by the pristine MFI zeolite and Cu-impregnated counterparts were estimated using DFT calculations. For the DFT calculations, we considered dry CST feed conditions (denoted by no water solvation; NWS) and wet CST feed conditions (denoted by water solvation only (WS_{0w}) and water solvation with one or two explicitly adsorbed water molecules (WS_{1w} or WS_{2w}, respectively)) in H^+-, Cu^+-, Cu^{2+}-MFI 46 T cluster models (Fig. 5c-e and S24 and Table S6). The binding energies of water molecules under the dry and wet feed conditions are shown in Fig. 5c; apparently, coordination to Cu^{2+} ions resulted in binding affinity or strength (indicated by the absolute value of binding energies) (-39.2 kcal·mol^{-1} for NWS and -17.3 kcal·mol^{-1} for WS_{2w}) stronger than those to H^+ ions (-28.6 kcal·mol^{-1} for NWS and -8.7 kcal·mol^{-1} for WS_{2w}) and Cu^+ ions (-32.6 kcal·mol^{-1} for NWS and -9.5 kcal·mol^{-1} for WS_{2w}), regardless of the absence or presence of the adsorbed water molecules. However, the binding energies of propene under dry conditions (NWS) shown in Fig. 5d indicate the preferential propene adsorption onto both Cu^+ and Cu^{2+} ions (-52.1 and -45.2 kcal·mol^{-1}, respectively) than H^+ ions (-23.6 kcal·mol^{-1}). Nevertheless, it was noted that the binding affinity of propene to H^+ ions was relatively high, suggesting that the pristine MFI zeolite could show modest propene adsorption under dry conditions (Figs. S19a1, S20a1, and S21a2-c2). Thus, the binding energies of propene on Cu^+ and Cu^{2+} ions suggest their roles in effective propene adsorption; the extent of adsorption gradually increased with increase in Cu content (Figs. S19a1-f1, S20a1-f1, and S21a2-c2). However, as shown in Figs. 2a, 4a, S17, S18, and S21a1-c1, under wet conditions (10 vol% water vapor), Cu(0) with H^+ ions alone could not adsorb propene at all and this can be attributed to the weaker binding affinity of H^+ ions toward propene under wet conditions (the binding energies for WS_{0w}, WS_{1w}, and WS_{2w} were -14.1, -13.4, and -13.6 kcal·mol^{-1}, respectively). Intriguingly, the absolute value of the binding energy of propene to Cu^{2+} ions was much smaller for WS_{2w} (-16.1 kcal·mol^{-1} vs. -41.9 kcal·mol^{-1} for WS_{0w} and -33.4 kcal·mol^{-1} for WS_{1w}). In contrast, the corresponding binding energies for Cu^+ ions were rather insensitive to the addition of explicit water molecules (the corresponding energies for WS_{0w}, WS_{1w}, and WS_{2w} were -47.9, -39.8, and -37.8 kcal·mol^{-1}, respectively). The binding energies of each cation species toward propene indicated that Cu^+ ions, not Cu^{2+} ions, were key to determining propene adsorption under wet conditions, thus highlighting the critical roles of Cu^+ ions in the experimentally obtained correlations shown in Fig. 4b1-b2 and c1-c2. As inferred from the high binding energies of CO on Cu^+ ions comparable to that of propene (Fig. S25), CO in the CST feed will disfavor the adsorption of propene and, thus, decreased the total amount of adsorbed propene (Fig. S21c1-c2), apparently owing to the competitive adsorption between CO and propene on to the same Cu^+ ions.

For toluene adsorption, the absolute values of the binding energies were sufficiently high, regardless of the cation species (Fig. 5e). In particular, they were higher than those for propene adsorption under both dry and wet conditions (Fig. 5d-e). Notably, all Cu-impregnated MFI zeolites showed marked toluene adsorption and, thus, total HC adsorption (Figs. S19b2-f2 and b3-f3 and S20b2-f2 and b3-f3 under dry conditions, and Figs. S17b2-f2 and b3-f3 and S18b2-f2 and b3-f3 under wet conditions). Indeed, even Cu(0) could adsorb toluene in both the CST and breakthrough tests under wet conditions (Fig. 2c, S6a2, S17a2, and S18a2), as expected from the strong toluene adsorption by the zeolite structure [15,70,71].

4.6. Oxidation ability of the Cu-impregnated MFI zeolites

Because CST performance is a complicated function of HC adsorption and oxidation, oxidation tests were required to analyze independently the effect of the oxidation ability of HC traps on the performance. Thus, the HC oxidation abilities of all Cu-impregnated MFI zeolites (i.e., Cu(x), x = 1, 3, 5, 7, and 10) at 300 °C were investigated (Fig. S26). As a result, we found that oxidation reactions occurred to a large extent when a large amount of Cu was loaded into the MFI zeolite. During CST, Cu(x) (x = 1 and 3) showed low oxidation ability in contrast to Cu(x) (x = 5, 7, and 10), which showed marked HC oxidation (Fig. S8). Interestingly, Cu(5) showed better propene adsorption ability than Cu(7) (Fig. 4a2), though the latter showed a slightly higher CST efficiency (Fig. 2 f). Thus, the HC oxidation abilities were thoroughly investigated at 70, 110, 160, 210, 240, 270, and 300 °C (see Figs. 6a2-b2, S27, and S28). For a better comparison, the CST performance and oxidation test results (especially for propene) of Cu(5) and Cu(7) are displayed side-by-side in Fig. 6a1-a2 and b1-b2. Furthermore, the results for CuO(7)/SiO$_2$ (all oxidation test results for Cu(7)/SiO$_2$ are shown in Fig. S29) are included as references at the bottom of Fig. 6.

It was noted that at low temperatures (70 and 110 °C), only HC adsorption occurred until ca. 20–25 min, after which no oxidation occurred, as reflected by identical inlet and outlet concentrations. However, upon further increasing the temperature to 160 °C, slight oxidation was observed at the expense of a decreased adsorption ability. Further, the oxidation abilities of both Cu(5) and Cu(7) monotonically increased with increasing temperature (Fig. 6a2-b2). As observed in Fig. 2 f, both Cu(5) and Cu(7) showed marked CST efficiencies; the amounts of adsorbed HCs at low temperature (e.g., 110 °C) were larger for Cu(5), whereas the oxidation performance was better for Cu(7) at sufficiently high temperatures ($\geq$ 160 °C). This clearly suggested that Cu(7) favored HC oxidation and this can be ascribed to the higher number of the CuO particles, which accounted for effective HC oxidation. In contrast, CuO(7)/SiO$_2$ did not exhibit HC adsorption or oxidation abilities up to approximately 300 °C (Fig. 6c2). This indicated that the large CuO particles in CuO(7)/SiO$_2$ were not appropriate for HC adsorption or oxidation [25]. Consequently, a large number of tiny CuO particles ($\leq$ ca. 4 nm) on the outer surface of the Cu-impregnated MFI zeolites (Fig. 1b and S4) were desirable for effective HC oxidation at low temperatures (less than 300 °C, after which the TWC is thermally activated).

4.7. Physicochemical properties of hydrothermally treated Cu-impregnated MFI zeolites

Because the HC trap is exposed to fluctuating temperatures and copious amounts of water vapor under real driving conditions, hydrothermal stability while retaining HC trapping performance under cold-start conditions is required. Therefore, we investigated the structural changes in the hydrothermally treated samples (Cu(x)_HT; x = 0, 1, 3, 5, 7, and 10) using XRD analyses. As shown in Fig. S30a, the XRD peak intensities representing the MFI zeolite structure decreased monotonically with increase in Cu content. In addition, in Fig. S30, the reflections corresponding to the aforementioned large CuO particles were observed at ca. 35.5° and 39° (marked by▼) in the XRD patterns of the high Cu content samples (Cu(x)_HT; x = 5, 7, and 10). The XRD patterns of Cu(x)_HT suggested that at high Cu loadings, the structure of the zeolite support was damaged by hydrothermal treatment (HT), though CuO particles (> 4 nm) were not significantly changed. Furthermore, the TEM images of Cu(x)_HT (x = 0, 1, 3, 5, 7, and 10) in Fig. S31 indicated that at a Cu content equal to or higher than 5 wt%, the tiny CuO particles on the outer surface of the MFI zeolite or other Cu species affected the overall structure of the zeolite [72] and created holes (ca. 10–30 nm), as indicated by blue arrows in Fig. S31d2-f2). Next, Ar physisorption experiments on Cu(x)_HT (x = 0, 1, 3, 5, 7, and 10) were conducted (Fig. S32); detailed information is given in Table S5. The presence of holes indicated by the TEM results was confirmed by the Barrett-Joyner-Halenda (BJH) method (Fig. S33); specifically, the number of mesopores decreased with increase in Cu content. In more detail, the number of mesopores in the range of ca. 2–10 nm sharply decreased with increase in Cu content and, interestingly, such mesopores were not found in Cu(x)_HT (x = 5, 7, and 10). Instead, much
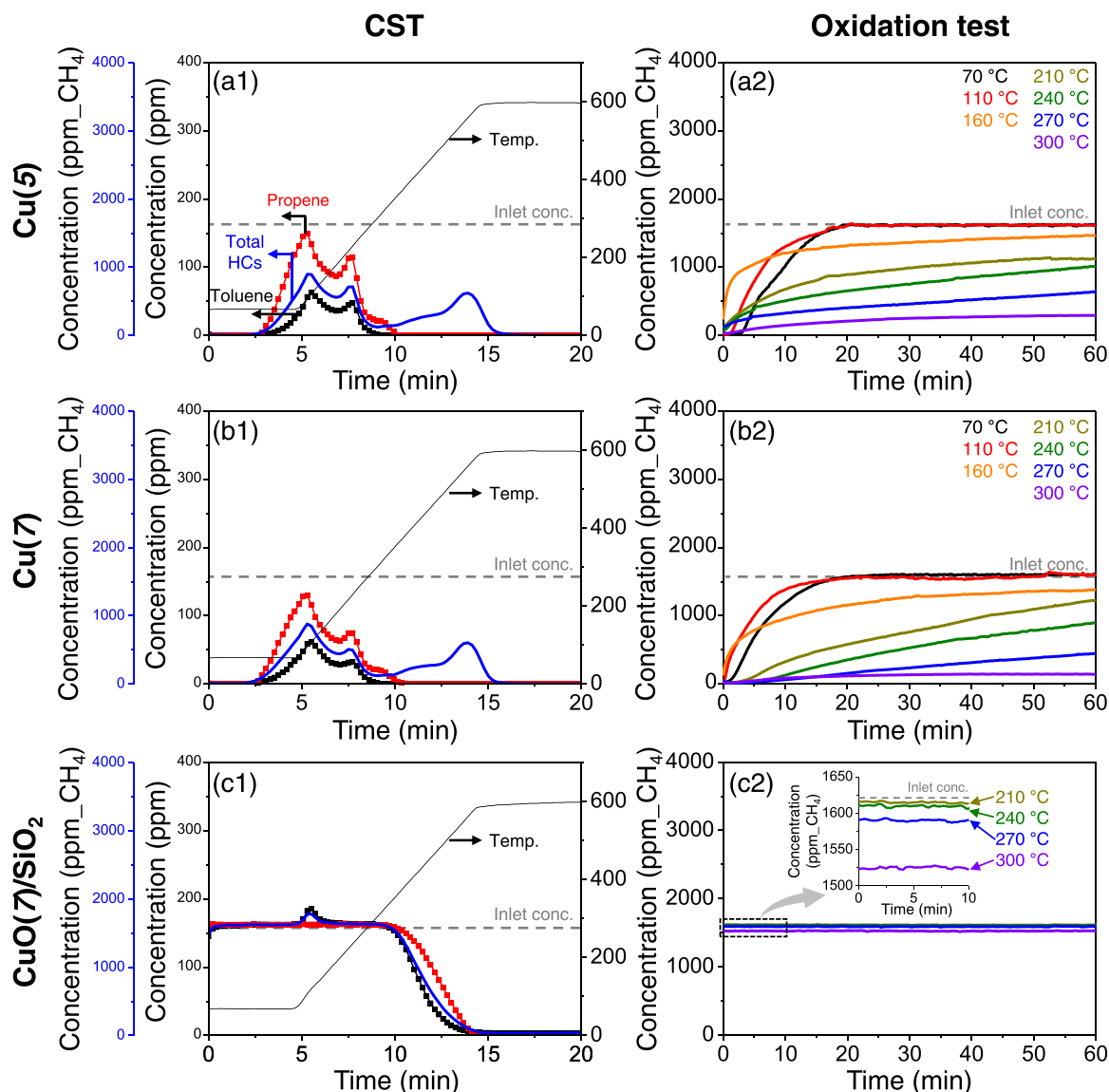
Fig. 6. (a1)-(c1) CST and (a2)-(c2) oxidation test results of (a1)-(a2) Cu(*5*), (b1)-(b2) Cu(*7*), and (c1)-(c2) CuO(*7*)/SiO₂. For comparison, in (a1)-(c1), the exit concentrations of propene and toluene acquired from the MS analyses and those of total HCs (in terms of CH₄) acquired from the GC analyses are displayed together. In (a2)-(c2), the exit concentrations of total HCs in terms of CH₄ were recorded at different temperatures; for the oxidation tests, the CST feed was used for 60 min.

larger mesopores that were consistent with the holes observed in the TEM images in Fig. S31d2-f2 were dominant in the samples with high Cu content (Cu(*x*)_HT; *x* = 5, 7, and 10). In addition, the number of zeolitic micropores of Cu(*x*)_HT decreased monotonically with increase in Cu content (Fig. S34). This was consistent with the XRD results as a function of the Cu content (as shown in Fig. S30a, all XRD peak intensities representing MFI structure decreased).

Furthermore, we obtained ²⁷Al (Fig. S35) and ²⁹Si MAS NMR (Fig. S36) spectra to track any structural changes after HT (supplemental discussion regarding the ²⁷Al and ²⁹Si MAS NMR characterization is provided in Subsection S2.9). Two ²⁷Al MAS NMR peaks of the fresh Cu-impregnated MFI zeolites at ca. 54–57 (representing tetrahedral Al sites) and 0 ppm (representing octahedral Al sites) weakened with increase in Cu content [73]. In contrast, the NMR peak around 30 ppm, which could be attributed to penta-coordinated Al sites, emerged in the spectra of Cu (*0*)_HT and Cu(*1*)_HT, probably as a result of the HT-induced zeolite structural changes [74–76]. Notably, Cu(*3*)_HT showed the highest ²⁷Al MAS NMR peak at ca. 54 ppm (Fig. S35b). In addition, the ²⁹Si MAS NMR spectra in Fig. S35 show that the peak corresponding to 3Si(1Al) in Cu(*0*) became very weak after HT, whereas it did not decrease as much

for the Cu-impregnated MFI zeolites. This can be attributed to Al leaching from the tetrahedral positions in Cu(*0*), as supported by the formation of penta-coordinated Al³⁺ ions in Fig. S35. In contrast, the Cu-impregnated MFI zeolites showed a monotonic decrease in both ²⁷Al and ²⁹Si MAS NMR peak intensities after HT. This indicates that the Cu species in the Cu-impregnated MFI zeolites plausibly lowered their structural stability after HT.

4.8. CST performances of Cu-impregnated MFI zeolites and their correlation with Cu⁺ ions

Having obtained an understanding of the physicochemical properties of Cu(*x*)_HT, we also investigated their CST performances (the corresponding CST results, adsorbed amounts, and CST efficiencies are shown in Figs. S37-S38 and additional discussion about the amount of adsorbed hydrocarbons in the fresh and HT samples is provided in Subsection S2.10). The propene adsorption abilities considerably decreased after HT; 0.0517–0.0081 mmol•g⁻¹ for Cu(*5*), 0.0494–0.0078 mmol•g⁻¹ for Cu(*7*), and 0.0299–0.0039 mmol•g⁻¹ for Cu(*10*) (Fig. S37b). In contrast, the performance of Cu(*3*) was not significantly affected by HT and

propene adsorption was only reduced from 0.0228 to 0.0143 mmol•g^{-1}, as shown in Fig. S37b. In addition, Cu(*1*) also maintained its original, but minimal adsorption capacity for propene (0.0057–0.0058 mmol•g^{-1} in Fig. S37b). Overall, Cu(*3*)_HT showed the highest propene adsorption ability among the hydrothermally treated samples. In particular, we noticed that Cu(*x*)_HT (*x* = 1 and 3), which had relatively low Cu contents, could adsorb toluene for up to 5 min. Thus, we could conclude that the structural stability of the Cu-impregnated MFI zeolite was reduced by the larger or excessive Cu loadings [25,77–79], as reflected by the poor CST performance of Cu(*x*)_HT (*x* = 5, 7, and 10; Fig. S38). Accordingly, their toluene adsorption ability, which was mainly related to the intact zeolite structure regardless of its cation form, diminished considerably (Fig. 2d and S37d). In summary, Cu(*3*) exhibited the most effective HC-trap performance after HT (Fig. S37f), though Cu(*5*) and Cu(*7*) showed the best HC-trap performance among the fresh samples (Fig. 2 f).

Finally, as done for the fresh samples, CO-adsorption FT-IR analyses were conducted for the hydrothermally treated samples. For Cu(*x*)_HT, we attempted to correlate the CO-adsorption FT-IR spectra with the amount of adsorbed propene. In Fig. 7a-b, the FT-IR peaks corresponding to Cu$^+$-CO in the hydrothermally treated Cu-impregnated MFI zeolites followed the trend observed for the fresh sample shown in Fig. 3b1-b2, though Cu(*3*)_HT instead of Cu(*5*)_HT yielded the most intense FT-IR peaks. Indeed, these results were consistent with that obtained from the NMR technique; Cu(*3*)_HT had the highest ^{27}Al MAS NMR peak at ca. 54 ppm (Fig. S35b). These indicate that the active sites for HC adsorption were well preserved in Cu(*3*) after HT, whose Cu content (3 wt%) was optimal. Accordingly, a linear regression between the specific absorbance area of the CO-adsorption FT-IR peaks and the amount of adsorbed propene was observed for Cu(*x*)_HT (Fig. 7b-c). Crucially, the linear relationship to account for the propene adsorption and Cu$^+$ ion content held well, as did that observed for the fresh samples (Fig. 4c1-c2). In addition, we found that the structural degradation monotonically decreased with increase in Cu loading (Table S5 and Fig. S39a), as relevant to Cu dislocation/migration and/or formation of copper aluminates during HT [72,80,81]. Despite the highest propene adsorption capacity in Cu(*5*), the structural degradation was not likely pronounced for an optimal Cu content (here, Cu(*3*)_HT), thus maintaining the largest amount of Cu$^+$ ions among the HT samples (Fig. 7 and S39b) and, accordingly, allowing for the highest propene adsorption capacity

(Fig. 7, S37-S38, and S40). Finally, it was noted that the HC-trap performance of the Cu(*3*)_HT sample was the highest, apparently because of the effective, coupled contribution of HC adsorption (Cu$^+$ ions and high degree of the textural/structural integrity; Fig. 7 and S32-S36) and oxidation (tiny CuO particles; Figs. S30-S31), whereas higher Cu contents reduced the original physicochemical properties during hydrothermal treatment (Fig. 7 and S30-S36) and, thus, HC-trap performance considerably (Fig. S37f).

5. Conclusions

In this study, a cold-start HC trap was prepared using a wet impregnation method with different Cu contents (up to 10 wt%). The resulting samples contained Cu cations inside the MFI zeolite owing to ion exchange, while tiny CuO particles were formed on the outer surface. The CST performance showed that the HC trap had the highest propene adsorption and CST efficiency when the copper loading was approximately 5–7 wt%. Furthermore, FT-IR analyses using multiple probe molecules (NO and CO) allowed for effective speciation and quantification of the Cu moieties in Cu-impregnated MFI zeolites. The complementary IR analyses indicated that the contents of both Cu$^+$ and Cu^{2+} ions increased with increase in Cu content, but decreased after a nominal Cu loading of 5 wt%.

Despite the linear correlation between the number of Cu cations and propene adsorption, we could not experimentally determine which Cu species (Cu$^+$ or Cu^{2+} ions) was key to the adsorption of propene during CST. To the best of our knowledge, we, for the first time, used a computational method based on a proton- or Cu-cation-containing MFI zeolite model to complement the experimental investigation and verify the effect of cation types. The binding energies for the key species obtained from DFT calculations revealed that the Cu$^+$ ions (not Cu^{2+} ions) were key to determining the adsorption of propene under wet conditions (10 vol% water vapor). In addition to understanding the roles of Cu cations in the HC adsorption, we further investigated the oxidation abilities of the Cu-impregnated MFI zeolites because this, along with HC adsorption, contributed to the HC removal in a complicated manner. The oxidation tests of Cu(*5*) and Cu(*7*) at various temperatures in the range of 70–300 °C further revealed that despite the slightly lower propene adsorption capacity, Cu(*7*) was more effective for oxidizing hydrocarbons, apparently because of the large quantity of CuO particles that
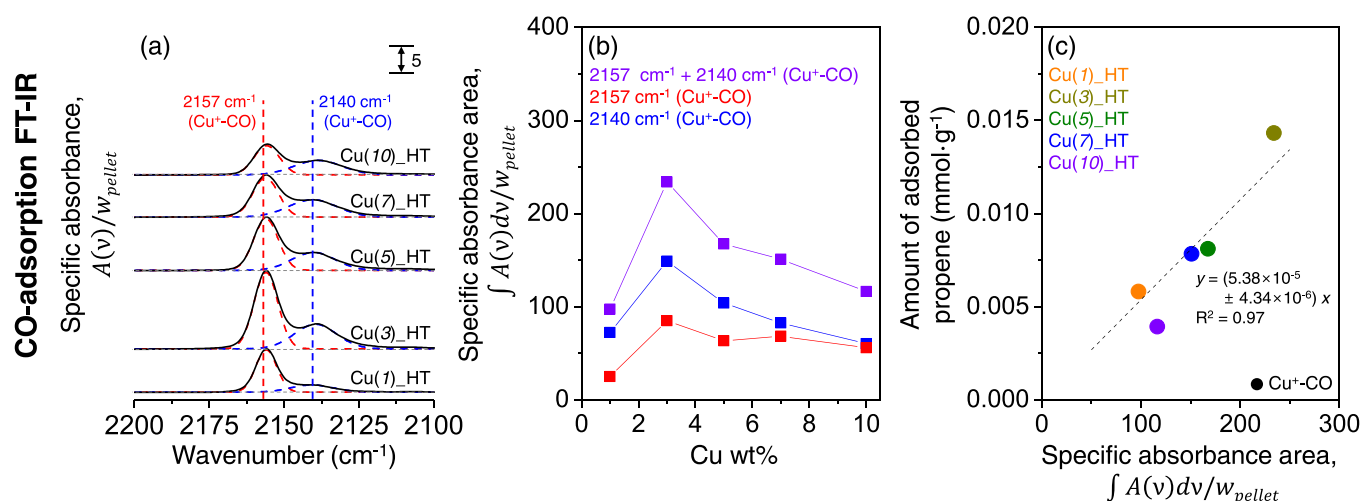
Fig. 7. (a) FT-IR spectra and (b) the corresponding absorbance areas of Cu(*x*)_HT (*x* = 1, 3, 5, 7, and 10) obtained using CO probe molecules. In (a), all spectra in the range of ca. 2120–2165 cm^{-1} were deconvoluted using the peaks around ν_{max} = 2157 cm^{-1} (Cu$^+$-CO; indicated by the red-dashed line) and ν_{max} = 2140 cm^{-1} (other Cu$^+$-CO; indicated by the blue-dashed line). All deconvoluted peaks in (a) were fitted with Gaussian distribution curves. In (b), the summation of the two specific absorbance areas owing to Cu$^+$-CO is marked in violet. In (c), the amounts of adsorbed propene are presented as a function of the specific absorbance areas, along with the linear regression plot. In (c), the specific absorbance areas corresponding to Cu$^+$-CO were obtained from the summation of the two specific absorbance areas owing to Cu$^+$-CO in (b).

accounted for effective HC oxidation.

However, HT at 800 °C in the presence of 10 vol% of water vapor for 12 h decreased the HC-trap performance considerably because this HT condition degraded or collapsed the original zeolite structure. Nevertheless, the degree of structural degradation/collapse depended on the Cu content. Specifically, Cu(*5*) and Cu(*7*) exhibited the highest CST performance in the fresh state, whereas after HT, Cu(*3*)_HT was the most effective for HC trapping. Thus, an optimal Cu content was required for the desired formation of Cu cations and CuO particles because the proper Cu species distribution led to the initial and long-term marked HC-trap performance. Furthermore, such Cu species (in particular, Cu cations incorporated into the zeolite framework) should be preserved to secure long-term HC-trap performance and the Cu species were strongly related to the zeolite structural robustness. These results suggested the importance of the active Cu species and the optimization of their contents in design of practical zeolite-based HC traps. To the best of our knowledge, the unprecedented, complementary interpretation of the experimental and theoretical results disclosed the key role of Cu^+ ions in propene adsorption under stoichiometric CST feed conditions. In addition, the use of MFI zeolites having a higher Si/Al ratio for Cu impregnation will be a good follow-up task, as the corresponding study will result in comprehensive understanding of the roles of Cu species.

CRediT authorship contribution statement

Jinseong Kim: Conceptualization, Visualization, Data curation, Formal analysis, Investigation, Writing – original draft, Writing – review & editing. **Jaehee Shim**: Visualization, Investigation, Data curation, Writing – original draft. **Jin Chul Kim**: Visualization, Investigation, Data curation, Writing – original draft. **Eunhee Jang**: Visualization, Investigation, Data curation. Formal analysis. **Jeong Hyeon Lee**: Visualization, Investigation, Data curation. **Hionsuck Baik**: Investigation, Data curation. **Chun Yong Kang**: Resources, Validation. **Chang Hwan Kim**: Resources, Validation. **Kwan-Young Lee**: Resources, Validation. Writing – review & editing. **Sang Kyu Kwak**: Supervision, Validation, Funding acquisition, Investigation, Writing – review & editing. **Jungkyu Choi**: Project administration, Conceptualization, Methodology, Supervision, Writing – original draft, Writing – review & editing, Funding acquisition, Investigation.

Declaration of Competing Interest

The authors declare that they have no known competing financial interests or personal relationships that could have appeared to influence the work reported in this paper.

Data Availability

Data will be made available on request.

Acknowledgements

Appendix A. Supporting information

References

[1] A. Getsoian, J.R. Theis, W.A. Paxton, M.J. Lance, C.K. Lambert, Remarkable improvement in low temperature performance of model three-way catalysts through solution atomic layer deposition, Nat. Catal. 2 (2019) 614–622.

[2] W. Lang, P. Laing, Y.S. Cheng, C. Hubbard, M.P. Harold, Co-Oxidation of CO and propylene on Pd/CeO2-ZrO2 and Pd/Al2O3 monolith catalysts: a light-off, kinetics, and mechanistic study, Appl. Catal. B-Environ. 218 (2017) 430–442.

[3] Y. Jing, Z.X. Cai, C. Liu, T. Toyao, Z. Maeno, H. Asakura, S. Hiwasa, S. Nagaoka, H. Kondoh, K. Shimizu, Promotional effect of La in the Three-way catalysis of La-loaded Al2O3-supported Pd catalysts (Pd/La/Al2O3), ACS Catal. 10 (2020) 1010–1023.

[4] R.J. Farrauto, M. Deeba, S. Alerasool, Gasoline automobile catalysis and its historical journey to cleaner air, Nat. Catal. 2 (2019) 603–613.

[5] J. Wan, J.S. Lin, X.L. Guo, T. Wang, R.X. Zhou, Morphology effect on the structure-activity relationship of Rh/CeO2-ZrO2 catalysts, Chem. Eng. J. 368 (2019) 719–729.

[6] H. Jeong, O. Kwon, B.S. Kim, J. Bae, S. Shin, H.E. Kim, J. Kim, H.J. Lee, Highly durable metal ensemble catalysts with full dispersion for automotive applications beyond single-atom catalysts, Nat. Catal. 3 (2020) 368–375.

[7] A. Papavasiliou, E.G. Deze, S.K. Papageorgiou, Z. Sideratou, N. Boukos, E. Poulakis, C.J. Philippopoulos, A. Glisenti, T.V. Everbroeck, P. Cool, F.K. Katsaros, A. Hyperbranched, Polymer synthetic strategy for the efficient fixation of metal species within nanoporous structures: application in automotive catalysis, Chem. Eng. J. 421 (2021), 129496.

[8] Y. Ryou, J. Lee, S.J. Cho, H. Lee, C.H. Kim, D.H. Kim, Activation of Pd/SSZ-13 catalyst by hydrothermal aging treatment in passive NO adsorption performance at low temperature for cold start application, Appl. Catal. B-Environ. 212 (2017) 140–149.

[9] J. Lee, J.R. Theis, E.A. Kyriakidou, Vehicle emissions trapping materials: successes, challenges, and the path forward, Appl. Catal. B-Environ. 243 (2019) 397–414.

[10] S.P. Elangovan, M. Ogura, Y. Zhang, N. Chino, T. Okubo, Silicoaluminophosphate molecular sieves as a hydrocarbon trap, Appl. Catal. B-Environ. 57 (2005) 31–36.

[11] M. Navlani-Garcia, F.J. Varela-Gandia, A. Bueno-Lopez, D. Cazorla-Amoros, B. Puertolas, J.M. Lopez, T. Garcia, D. Lozano-Castello, BETA zeolite thin films supported on honeycomb monoliths with tunable properties as hydrocarbon traps under cold-start conditions, Chemsuschem 6 (2013) 1467–1477.

[12] A. Westermann, B. Azambre, G. Finqueneisel, P. Da Costa, F. Can, Evolution of unburnt hydrocarbons under "cold-start" conditions from adsorption/desorption to conversion: on the screening of zeolitic materials, Appl. Catal. B-Environ. 158 (2014) 48–59.

[13] B. Puertolas, L. Garcia-Andujar, T. Garcia, M.V. Navarro, S. Mitchell, J. Perez-Ramirez, Bifunctional Cu/H-ZSM-5 zeolite with hierarchical porosity for hydrocarbon abatement under cold-start conditions, Appl. Catal. B-Environ., 154-155 (2014) 161–170.

[14] J. Luo, R.W. McCabe, M.A. Dearth, R.J. Gorte, Transient adsorption studies of automotive hydrocarbon traps, AIChE J. 60 (2014) 2875–2881.

[15] N.R. Burke, D.L. Trimm, R.F. Howe, The effect of silica: alumina ratio and hydrothermal ageing on the adsorption characteristics of bea zeolites for cold start emission control, Appl. Catal. B-Environ. 46 (2003) 97–104.

[16] D.S. Lafyatis, G.P. Ansell, S.C. Bennett, J.C. Frost, P.J. Millington, R.R. Rajaram, A. P. Walker, T.H. Ballinger, Ambient temperature light-off for automobile emission control, Appl. Catal. B-Environ. 18 (1998) 123–135.

[17] K. Ramanathan, C.K. Koch, S.H. Oh, Kinetic modeling of hydrocarbon adsorbers for gasoline and ethanol fuels, Chem. Eng. J. 207 (2012) 175–194.

[18] A. Takahashi, T. Tomita, T. Hiramatsu, K. Suzuki, M. Matsukata, Highly heat resistant β-zeolite and absorbent for automobile exhaust gas purification and adsorbent for automobile exhaust gas purification, US 6 (150 B2) (2001) 294.

[19] J.M. Lopez, M.V. Navarro, T. Garcia, R. Murillo, A.M. Mastral, F.J. Varela-Gandia, D. Lozano-Castello, A. Bueno-Lopez, D. Cazorla-Amoros, Screening of different zeolites and silicoaluminophosphates for the retention of propene under cold start conditions, Microporous Mesoporous Mater. 130 (2010) 239–247.

[20] Q.J. Yu, X.Y. Chen, A. Bhat, X.L. Tang, H.H. Yi, X.C. Lin, J.W. Schwank, Activation of passive NOx adsorbers by pretreatment with reaction gas mixture, Chem. Eng. J. 399 (2020), 125727.

[21] M. Ambast, S.A. Malamis, M.P. Harold, Coupled uptake and conversion of $C_{12}H_{26}$ and NO on Pd/SSZ-13: experiments and modeling, Chem. Eng. J. 423 (2021), 129958.

[22] M. Navlani-Garcia, B. Puertolas, D. Lozano-Castello, D. Cazorla-Amoros, M. V. Navarro, T. Garcia, CuH-ZSM-5 as hydrocarbon trap under cold start conditions, Environ. Sci. Technol. 47 (2013) 5851–5857.

[23] H. Kim, E. Jang, Y. Jeong, J. Kim, C.Y. Kang, C.H. Kim, H. Baik, K.Y. Lee, J. Choi, On the synthesis of a hierarchically-structured ZSM-5 zeolite and the effect of its physicochemical properties with Cu impregnation on cold-start hydrocarbon trap performance, Catal. Today 314 (2018) 78–93.

[24] J. Kim, E. Jang, Y. Jeong, H. Baik, S.J. Cho, C.Y. Kang, C.H. Kim, J. Choi, A Cu-impregnated ZSM-5 zeolite for active cold start hydrocarbon removal: cation-type-dependent cu species and their synergetic HC adsorption/oxidation functions, Chem. Eng. J. 430 (2022), 132552.

[25] E. Jang, L. Choi, J. Kim, Y. Jeong, H. Baik, C.Y. Kang, C.H. Kim, K.Y. Lee, J. Choi, A copper-impregnated BEA zeolite for adsorption and oxidation of aromatic species during vehicle cold starts, Appl. Catal. B-Environ. 287 (2021), 119951.

[26] B. Puertolas, M. Navlani-Garcia, T. Garcia, M.V. Navarro, D. Lozano-Castello, D. Cazorla-Amoros, Optimizing the performance of catalytic traps for hydrocarbon abatement during the cold-start of a gasoline engine, J. Hazard. Mater. 279 (2014) 527–536.

[27] B. Puertolas, M. Navlani-Garcia, J.M. Lopez, T. Garcia, R. Murillo, A.M. Mastral, M. V. Navarro, D. Lozano-Castello, A. Bueno-Lopez, D. Cazorla-Amoros, Molecular simulation design of a multisite solid for the abatement of cold start emissions, Chem. Commun. 48 (2012) 6571–6573.

[28] S.K. Park, V. Kurshev, Z.H. Luan, C.W. Lee, L. Kevan, Reaction of NO with copper ions in Cu(II)-exchanged ZSM-5 zeolite: electron spin resonance, electron spin echo modulation and fourier transform infrared spectroscopy, Microporous Mesoporous Mater. 38 (2000) 255–266.

[29] A. Sultana, T. Nanba, M. Haneda, M. Sasaki, H. Hamada, Influence of Co-cations on the formation of Cu^+ species in Cu/ZSM-5 and Its Effect on selective catalytic reduction of NOx with NH_3, Appl. Catal. B-Environ. 101 (2010) 61–67.

[30] K.G. Wilshier, P. Smart, R. Western, T. Mole, T. Behrsing, Oligomerization of propene over H-ZSM-5 zeolite, Appl. Catal. 31 (1987) 339–359.

[31] J.Y. Yan, G.D. Lei, W.M.H. Sachtler, H.H. Kung, Deactivation of Cu/ZSM-5 catalysts for lean Nox reduction: characterization of changes of Cu state and zeolite support, J. Catal. 161 (1996) 43–54.

[32] A. Gervasini, C. Picciau, A. Auroux, Characterization of copper-exchanged ZSM-5 and ETS-10 catalysts with low and high degrees of exchange, Microporous Mesoporous Mater., 35- 6 (2000) 457–469.

[33] J. Sarkany, J.L. Ditri, W.M.H. Sachtler, Redox chemistry in excessively ion-exchanged Cu/Na-ZSM-5, Catal. Lett. 16 (1992) 241–249.

[34] X.L. Song, N. Jiang, Y.K. Li, D.Y. Xu, G.Z. Qiu, Synthesis of CeO_2-coated SiO_2 nanoparticle and dispersion stability of its suspension, Mater. Chem. Phys. 110 (2008) 128–135.

[35] M.S. 2019, BIOVIA, Dassault Systèmes: San Diego, (2018).

[36] H. Sun, COMPASS: An Ab initio force-field optimized for condensed-phase applications - overview with details on alkane and benzene compounds, J. Phys. Chem. B 102 (1998) 7338–7364.

[37] B. Delley, An All-Electron, Numerical-method for solving the local density functional for polyatomic-molecules, J. Chem. Phys. 92 (1990) 508–517.

[38] B. Delley, From molecules to solids with the DMol^3, Approach, J. Chem. Phys. 113 (2000) 7756–7764.

[39] J.P. Perdew, K. Burke, M. Ernzerhof, Generalized gradient approximation made simple, Phys. Rev. Lett. 77 (1996) 3865–3868.

[40] A. Tkatchenko, M. Scheffler, Accurate molecular van der waals interactions from ground-state electron density and free-atom reference data, Phys. Rev. Lett. 102 (2009), 073005.

[41] A. Klamt, G. Schuurmann, COSMO: A new approach to dielectric screening in solvents with explicit expressions for the screening energy and its gradient, Chem. Soc., Perkin Trans. II (1993) 799–805.

[42] Y. Wongngwmaq, P. Kidkhunthod, U. Sukkha, S. Pengpanich, K.A. Thavornprasert, J. Phupanit, N. Kungwan, G. Feng, T. Keawin, S. Jungsuttiwong, Local structure elucidation and reaction mechanism of light naphtha aromatization over Ga embedded H-ZSM-5 zeolite: combined DFT and experimental study, Microporous Mesoporous Mater. 306 (2020), 110414.

[43] G. Barone, N. Armata, A. Prestianni, T. Rubino, D. Duca, D.Y. Murzin, Confined But-2-ene catalytic isomerization inside H-ZSM-5 models: a DFT study, J. Chem. Theory Comput. 5 (2009) 1274–1283.

[44] V. Shapovalov, A.T. Bell, Theoretical study of zeolite-catalyzed dimethoxymethane carbonylation to methyl methoxyacetate, J. Phys. Chem. C. 114 (2010) 17753–17760.

[45] M.S. Akhter, A.R. Chughtai, D.M. Smith, The structure of hexane soot I: Spectroscopic studies, Appl. Spectrosc. 39 (1985) 143–153.

[46] P. Da Costa, B. Moden, G.D. Meitzner, D.K. Lee, E. Iglesia, Spectroscopic and chemical characterization of active and inactive Cu species in NO decomposition catalysts based on Cu-ZSM5, Phys. Chem. Chem. Phys. 4 (2002) 4590–4601.

[47] M.A.C. Markovits, A. Jentys, M. Tromp, M. Sanchez-Sanchez, J.A. Lercher, Effect of location and distribution of Al Sites in ZSM-5 on the formation of Cu-Oxo clusters active for direct conversion of methane to methanol, Top. Catal. 59 (2016) 1554–1563.

[48] I. Sobczak, P. Decyk, M. Ziolek, M. Daturi, J.C. Lavalley, L. Kevan, A.A. Prakash, Physicochemical properties and catalytic activity of Cu-NbZSM-5 - a comparative study with Cu-AlZSM-5, J. Catal. 207 (2002) 101–112.

[49] E. Giamello, D. Murphy, G. Magnacca, C. Morterra, Y. Shioya, T. Nomura, M. Anpo, The interaction of NO with copper ions in ZSM5 - an EPR and IR investigation, J. Catal. 136 (1992) 510–520.

[50] H.J. Jang, W.K. Hall, J. dItri, Redox behavior of CuZSM-5 catalysts: FTIR investigations of reactions of adsorbed NO and CO, J. Phys. Chem. Solids 100 (1996) 9416–9420.

[51] C. Lamberti, S. Bordiga, M. Salvalaggio, G. Spoto, A. Zecchina, F. Geobaldo, G. Vlaic, M. Bellatreccia, XAFS, IR, and UV–vis Study of the Cu^I Environment in Cu^I-ZSM-5, J. Phys. Chem. B 101 (1997) 344–360.

[52] M. Iwamoto, Y. Hoshino, Assignment of nonclassical $[Cu(CO)_n]^+$ ($n = 1, 2$) complex ions in zeolite cages, Inorg. Chem. 35 (1996) 6918–6921.

[53] K.A. Tarach, M. Jablonska, K. Pyra, M. Liebau, B. Reiprich, R. Glaser, K. Gora-Marek, Effect of zeolite topology on NH_3-SCR activity and stability of Cu-exchanged zeolites, Appl. Catal. B-Environ. 284 (2021) 119752.

[54] G.L. Woolery, G.H. Kuehl, H.C. Timken, A.W. Chester, J.C. Vartuli, On the nature of framework bronsted and Lewis acid sites in ZSM-5, Zeolites 19 (1997) 288–296.

[55] G. Busca, FT-IR study of the surface of copper-oxide, J. Mol. Catal. 43 (1987) 225–236.

[56] E.V. Benvenutti, Y. Gushikem, C.U. Davanzo, Pyridine used as a probe for internal brønsted acid sites in pyrochlore antimony (V) oxide: an infrared spectroscopy study, Appl. Spectrosc. 46 (1992) 1474–1476.

[57] W.Q. Wu, E. Weitz, Modification of acid sites in ZSM-5 by ion-exchange: an in-situ FTIR study, Appl. Surf. Sci. 316 (2014) 405–415.

[58] J. Datka, E. Kukulska-Zajac, IR studies of the activation of C═C bond in alkenes by Cu^+ ions in zeolites, J. Phys. Chem. B 108 (2004) 17760–17766.

[59] F. Benaliouche, Y. Boucheffa, F. Thibault-Starzyk, In situ FTIR studies of propene adsorption over Ag- and Cu-Exchanged Y zeolites, Microporous Mesoporous Mater. 147 (2012) 10–16.

[60] K. Horiguchi, A. Itadani, K. Uematsu, K. Toda, M. Sato, IR spectroscopic detection of the propene species formed via the interaction of copper-ion-exchanged MFI-type zeolite with propane at 573 K, Vib. Spectrosc. 106 (2020), 103016.

[61] F. Giordanino, P.N.R. Vennestrom, L.F. Lundegaard, F.N. Stappen, S. Mossin, P. Beato, S. Bordiga, C. Lamberti, Characterization of Cu-exchanged SSZ-13: a comparative FTIR, UV-Vis, and EPR Study with Cu-ZSM-5 and Cu-beta with Similar Si/Al and Cu/Al Ratios, Dalton Trans. 42 (2013) 12741–12761.

[62] R.A. Schoonheydt, Combined ESR-DRS spectroscopies of transition-metal ions and metal-ion clusters in zeolite, Phys. Chem. Solids 50 (1989) 523–539.

[63] Y. Zu, Z.S. Guo, J. Zheng, Y. Hui, S.H. Wang, Y.C. Qin, L. Zhang, H.H. Liu, X. H. Gao, L.J. Song, Investigation of Cu(I)-Y zeolites with different Cu/Al ratios towards the ultra-deep adsorption desulfurization: discrimination and role of the specific adsorption active sites, Chem. Eng. J. 380 (2020), 122319.

[64] B. Pereda-Ayo, U. De La Torre, M.J. Illan-Gomez, A. Bueno-Lopez, J.R. Gonzalez-Velasco, Role of the different copper species on the activity of cu/zeolite catalysts for SCR of NOx with NH_3, Appl. Catal. B-Environ. 147 (2014) 420–428.

[65] H. Wang, R.N. Xu, Y. Jin, R.D. Zhang, Zeolite structure effects on Cu active center, SCR performance and stability of Cu-zeolite catalysts, Catal. Today 327 (2019) 295–307.

[66] J. Datka, E. Kukulska-Zajac, P. Kozyra, IR and TPD studies of the interaction of alkenes with Cu^+ Sites in CuNaY and CuNaX zeolites of various Cu Content. The heterogeneity of Cu^+ Sites, J. Mol. Struct. 794 (2006) 261–264.

[67] Y.S. Bae, C.Y. Lee, K.C. Kim, O.K. Farha, P. Nickias, J.T. Hupp, S.T. Nguyen, R. Q. Snurr, High propene/propane selectivity in isostructural metal-organic frameworks with high densities of open metal sites, Angew. Chem. -Int. Ed. 51 (2012) 1857–1860.

[68] N. Lamia, M. Jorge, M.A. Granato, F.A.A. Paz, H. Chevreau, A.E. Rodrigues, Adsorption of propane, propylene and isobutane on a metal-organic framework: molecular simulation and experiment, Chem. Eng. Sci. 64 (2009) 3246–3259.

[69] A. Westermann, B. Azambre, M. Chebbi, A. Koch, Modification of Y faujasite zeolites for the trapping and elimination of a propene-toluene-decane mixture in the context of cold-start, Microporous Mesoporous Mater. 230 (2016) 76–88.

[70] Y. Kobatake, K. Momma, S.P. Elangovan, K. Itabashi, T. Okubo, M. Ogura, Super hydrocarbon reformer trap" for the complete oxidation of toluene using iron-exchanged beta-zeolite with a low silicon/aluminum ratio, Chemcatchem 8 (2016) 2516–2524.

[71] S.B. Kang, S. Kalamaras, V. Balakotaiah, W. Epling, Hydrocarbon trapping over Ag-beta zeolite for cold-start emission control, Catal. Lett. 147 (2017) 1355–1362.

[72] P.N.R. Vennestrøm, T.V.W. Janssens, A. Kustov, M. Grill, A. Puig-Molina, L. F. Lundegaard, R.R. Tiruvalam, P. Concepcion, A. Corma, Influence of lattice stability on hydrothermal deactivation of Cu-ZSM-5 and Cu-IM-5 zeolites for selective catalytic reduction of NOx by NH3, J. Catal. 309 (2014) 477–490.

[73] S. Brandenberger, O. Krocher, M. Casapu, A. Tissler, R. Althoff, Hydrothermal deactivation of Fe-ZSM-5 catalysts for the selective catalytic reduction of NO with NH3, Appl. Catal. B-Environ. 101 (2011) 649–659.

[74] J.H. Kwak, J.Z. Hu, D.H. Kim, J. Szanyi, C.H.F. Peden, Penta-coordinated Al^{3+} ions as preferential nucleation sites for BaO on gamma-Al_2O_3: an ultra-high-magnetic field ^{27}Al MAS NMR study, J. Catal. 251 (2007) 189–194.

[75] O. Lisboa, M. Sanchez, F. Ruette, Modeling extra framework aluminum (EFAL) formation in the zeolite ZSM-5 using parametric quantum and dft methods, J. Mol. Catal. A Chem. 294 (2008) 93–101.

[76] K. Khivantsev, N.R. Jaegers, L. Kovarik, M.A. Derewinski, J.H. Kwak, J. Szanyi, On the nature of extra-framework aluminum species and improved catalytic properties in steamed zeolites, Molecules 27 (2022) 2352.

[77] V. Houel, D. James, P. Millington, S. Pollington, S. Poulston, R. Rajaram, R. Torbati, A comparison of the activity and deactivation of Ag/Al_2O_3 and Cu/ZSM-5 for HC-SCR under simulated diesel exhaust emission conditions, J. Catal. 230 (2005) 150–157.

[78] D.W. Fickel, E. D'Addio, J.A. Lauterbach, R.F. Lobo, The ammonia selective catalytic reduction activity of copper-exchanged small-pore zeolites, Appl. Catal. B-Environ. 102 (2011) 441–448.

[79] H. Lee, I. Song, S.W. Jeon, D.H. Kim, Inter-particle migration of Cu ions in physically mixed Cu-SSZ-13 and H-SSZ-13 treated by hydrothermal aging, React. Chem. Eng. 4 (2019) 1059–1066.

[80] J.Y. Yan, W.M.H. Sachtler, H.H. Kung, Effect of Cu loading and addition of modifiers on the stability of Cu/ZSM-5 in lean NO_x reduction catalysis, Catal. Today 33 (1997) 279–290.

[81] X.W. Ye, J.E. Schmidt, R.P. Wang, I.K. van Ravenhorst, R. Oord, T.H. Chen, F. de Groot, F. Meirer, B.M. Weckhuysen, Deactivation of Cu-exchanged automotive-emission NH3-SCR catalysts elucidated with nanoscale resolution using scanning transmission X-ray microscopy, Angew. Chem. -Int. Ed. 59 (2020) 15610–15617.